JCB Journal of Cell Biology

ARTICLE

Transient septin sumoylation steers a Fir1-Skt5 protein complex between the split septin ring

Judith Müller[1], Monique Furlan[1], David Settele[1], Benjamin Grupp[1], and Nils Johnsson[1]

Ubiquitylation and phosphorylation control composition and architecture of the cell separation machinery in yeast and other eukaryotes. The significance of septin sumoylation on cell separation remained an enigma. Septins form an hourglass structure at the bud neck of yeast cells that transforms into a split septin double ring during mitosis. We discovered that sumoylated septins recruit the cytokinesis checkpoint protein Fir1 to the peripheral side of the septin hourglass just before its transformation into the double-ring configuration. As this transition occurs, Fir1 is released from the septins and seamlessly relocates between the split septin rings through synchronized binding to the scaffold Spa2. Fir1 binds and carries the membrane-bound Skt5 on its route to the division plane where the Fir1-Skt5 complex serves as receptor for chitin synthase III.

Introduction

The five mitotic septins of the yeast *Saccharomyces cerevisiae*, Cdc11, Cdc12, Cdc10, Cdc3, and Shs1, assemble into hetero-octameric rods that polymerize end to end into apolar filaments (Woods and Gladfelter, 2021; Marquardt et al., 2021). At the beginning of each cell cycle, septin filaments form a ring-like structure next to a previous division site through which the directed transport of secretory vesicles creates a new bud that grows and matures into the next daughter cell (Chiou et al., 2017; Pruyne and Bretscher, 2000; Chollet et al., 2020). The septin ring expands later into an hourglass structure in which paired septin filaments are closely aligned at the bud neck along the mother–bud axis (DeMay et al., 2011; Ong et al., 2014). The splitting of the hourglass into two rings prominently marks the beginning of cytokinesis. This transformation involves the loss of the paired filaments with a concomitant formation of new filaments perpendicular to the mother–bud axis (DeMay et al., 2011; Chen et al., 2020; Vrabioiu and Mitchison, 2006). The contracting actin myosin ring (AMR) subsequently pulls the newly exposed membrane between the two rings toward the center of the bud neck. Chitin synthase II (Chs2) simultaneously synthesizes a primary septum between the two sheets of the constricted plasma membrane. The concerted actions of chitin synthase III (Chs3) and the β-1,6 glucan synthase Fks1 layer a secondary septum upon the primary septum. Finally, the daughter cell releases hydrolases that remove the primary septum to separate both cells (Meitinger and Palani, 2016; Bhavsar-Jog and Bi, 2017; Onishi et al., 2013).

The split septin double ring (SSDR) performs two important functions during cytokinesis: first, it seals off the membrane of the cytokinesis compartment to keep the membrane-attached proteins within the SSDR (Dobbelaere and Barral, 2004; Wloka et al., 2011). Second, it serves as a platform from which proteins are sequentially released into the cleavage furrow to take part in the different steps of cell separation (Meitinger et al., 2013; Meitinger et al., 2011; Schneider et al., 2013; Fang et al., 2010).

The yeast septins Cdc11, Cdc3, and Shs1 are known to be sumoylated during mitosis and desumoylated shortly before cell separation (Johnson and Blobel, 1999; Takahashi et al., 1999). Sumoylation involves only a minority of the septins and is restricted to the peripheral region of the septin hourglass facing the mother cell (Johnson and Blobel, 1999). The precise timing of septin sumoylation and desumoylation is achieved by the successive export of the small ubiquitin-like modifier (SUMO, Smt3) ligase Siz1 and the Smt3 protease Ulp1 from the nucleus into the cytosol (Makhnevych et al., 2007; Takahashi et al., 2000, 2001; Johnson and Gupta, 2001). Both enzymes return to the nucleus before a new cell cycle starts (Elmore et al., 2011; Makhnevych et al., 2007; Lewis et al., 2007; Panse et al., 2003). Timing and location imply that septin sumoylation plays a role during cytokinesis. Although suggestive, the question of whether this elaborate modification cycle influences any of the functions of the septins remained open for more than 20 years.

The remarkable resilience of cell separation mechanisms in the face of both internal and external stresses suggests that the consecutive activities of cytokinesis are tightly coordinated.

[1]Department of Biology, Institute of Molecular Genetics and Cell Biology, Ulm University, Ulm, Germany.

Correspondence to Nils Johnsson: nils.johnsson@uni-ulm.de; Judith Müller: judith.mueller@uni-ulm.de.

Notably, cell separation should only proceed once AMR contraction and membrane closure have been successfully completed. Fir1, a novel checkpoint protein, was recently proposed to regulate this dependency by modulating the release of septum-degrading hydrolases into the extracellular space (Brace et al., 2019). Fir1 emerges at the division site shortly before cell separation, where it is believed to inhibit the kinase activity of Cbk1, a member of the nuclear Dbf2-related/large tumor suppressor (NDR/LATS) kinase family, known to facilitate the separation of mother and daughter cells (Brace et al., 2019; Bidlingmaier et al., 2001; Colman-Lerner et al., 2001; Weiss et al., 2002; Weiss 2012). Many aspects of this checkpoint mechanism are still not understood. Outstanding questions pertain to the mechanisms governing Fir1's localization to the bud neck and its ability to detect and correct errors in septum formation.

In this study, we show that the sumoylation of septins initiates a two-step targeting process that escorts Fir1 and Skt5 into the space between the SSDR where the Fir1-Skt5 complex serves as a receptor for Chs3 and promotes chitin synthesis during secondary septum formation.

Results

Sumoylation recruits Fir1 to the peripheral side of the septin hourglass

Fir1 is predicted to present multiple linear interaction motifs within a predominantly unfolded structure (Fig. 1 A; Brace et al., 2019; Grinhagens et al., 2020; Jumper et al., 2021). Fir1 binds to Smt3 through its SUMO-interacting motif (SIM) and was recently shown to localize to the bud neck during cell abscission (Hannich et al., 2005; Uzunova et al., 2007; Brace et al., 2019; Grinhagens et al., 2020). To test whether binding to Smt3 is required for Fir1's localization at the bud neck, we compared the cellular distribution of Fir1-GFP to a mutant of Fir1 that lacked residues 759–767 of the SIM ($Fir1_{\Delta SIM}$). Split-Ubiquitin (Split-Ub) analysis proofed that $Fir1_{\Delta SIM}$ specifically lost its interaction with Smt3 (Fig. 1 B). Fir1-GFP appeared at the bud neck 8–10 min before the septin ring splits and the AMR starts to contract (Fig. 1 C). It remained there for ∼18 min before it rapidly disappeared. $Fir1_{\Delta SIM}$-GFP could be detected at the bud neck 10 min later than the wild-type protein, but then showed a similar signal intensity and kinetic of disappearance (Fig. 1 C). Fir1-GFP first appeared as a ring at the mother side of the septin structure (Fig. 1 D). This ring then shifted between the SSDR during the hourglass transition and contracted as cytokinesis continued (Fig. 1 D; Brace et al., 2019). Position and timing of the Fir1 ring within the SSDR coincided with the ring-like structure of $Fir1_{\Delta SIM}$-GFP when it first appeared at the bud neck (Fig. 1 C and Fig. S1 A).

To find out whether septin sumoylation is required for the early appearance of Fir1 at the bud neck (phase I targeting), we measured the fluorescence intensity profiles of Fir1-GFP in cells lacking the SUMO ligase Siz1 (*siz1*Δ) or in the congenic strain EJY316, where all sumoylatable lysines were replaced by arginine (sepΔsumo; Table S2; Johnson and Gupta, 2001; Johnson and Blobel, 1999). The Fir1-GFP profiles of both mutants were nearly identical, and in their timing very similar to the profile of $Fir1_{\Delta SIM}$-GFP. Both lacked phase I targeting (Fig. 1 E). We conclude that sumoylated septins recruit Fir1 to the periphery of the septin ring shortly before it splits.

During AMR contraction, Fir1-GFP moves from its peripheral position between the SSDR (Fig. 1 D and Fig. S1 A; phase II targeting). Neither deleting the SIM in Fir1 nor preventing septin sumoylation delayed phase II targeting of Fir1-GFP (Fig. 1, C and E). However, the signal intensities of Fir1-GFP in *siz1*Δ or sepΔsumo cells during phase II targeting were substantially reduced when compared with its signal in wild type cells (Fig. 1 E and Fig. S1 C). These findings argue for a separate receptor that keeps Fir1 at the bud neck after desumoylation of the septins. The partial loss of Fir1 from the SSDR in sumoylation-deficient cells might imply that both targeting steps are somehow coupled.

The polarity scaffold Spa2 attaches Fir1 to the cleavage furrow

We performed a Split-Ub interaction screen to obtain a shortlist of candidate proteins that might anchor Fir1 at the bud neck during phase II targeting (Fig. 2 A and Fig. S2, Table S1; Hruby et al., 2011; Johnsson and Varshavsky, 1994). The polarisome scaffold Spa2 and other subunits of the polarisome were discovered as novel interaction partners of Fir1 (Fig. 2 A; Neller et al., 2015; Tcheperegine et al., 2005; Shih et al., 2005; Dünkler et al., 2021; Valtz and Herskowitz, 1996).

We considered Spa2 as a candidate receptor as it appeared at the bud neck at about the same time as $Fir1_{\Delta SIM}$ during phase II targeting (Fig. 2, B, C, and E; Fig. S3 A; Snyder, 1989). Accordingly, the deletion of Spa2 prevented Fir1-GFP from transferring into the SSDR and nearly abolished the bud neck signal of $Fir1_{\Delta SIM}$-GFP during both phases (Fig. 2, B, C, and E). Reciprocally, the deletion of Fir1 or the absence of septin sumoylation did not affect the distribution of Spa2 (Fig. S3 C). We conclude that the sumoylated septins recruit Fir1 to the bud neck during phase I targeting, whereas Spa2 acts as a Fir1 receptor during phase II targeting. A C-terminal fragment of Fir1 ($Fir1_{750-876}$) that starts within the predicted N-terminal β-strand of the SIM lacked phase I targeting and recapitulated the dynamic localization of Spa2-GFP at the bud neck (Fig. 2, D and E; Jumper et al., 2021). Similar to Spa2-Cherry, $Fir1_{750-876}$-GFP remained at the site of cell division and later transferred to the tip of the growing bud (Fig. 2 F). GFP-fusions of full-length Fir1 and most of its other variants localized to the bud tip at a significantly lower level, almost below the detection limit of our wide-field microscope (Fig. 2 F). The deletion of *SPA2* abolished the localization of $Fir1_{750-876}$-GFP equally and completely at bud neck and tip (Fig. 2, D–F; and Fig. S3 D), thus restricting the potential Spa2-binding site within the C-terminal 126 residues of Fir1.

Fir1 and Spa2 form a stable protein complex

A stretch within these C-terminal 126 residues of Fir1 is phylogenetically conserved (Fig. 1 A; Fuentes et al., 2022). Deleting this region ($Fir1_{\Delta 801-820}$) specifically abolished the interaction with Spa2 and caused the premature dissociation of $Fir1_{\Delta 801-820}$-GFP from the bud neck without affecting its initial phase I targeting (Fig. 3, A–C). The calculated fluorescence intensity profile of $Fir1_{\Delta 801-820}$-GFP was congruent with the profile of wild-type Fir1-GFP in *spa2*Δ cells (Fig. 3, B, C, and E) and complementary to

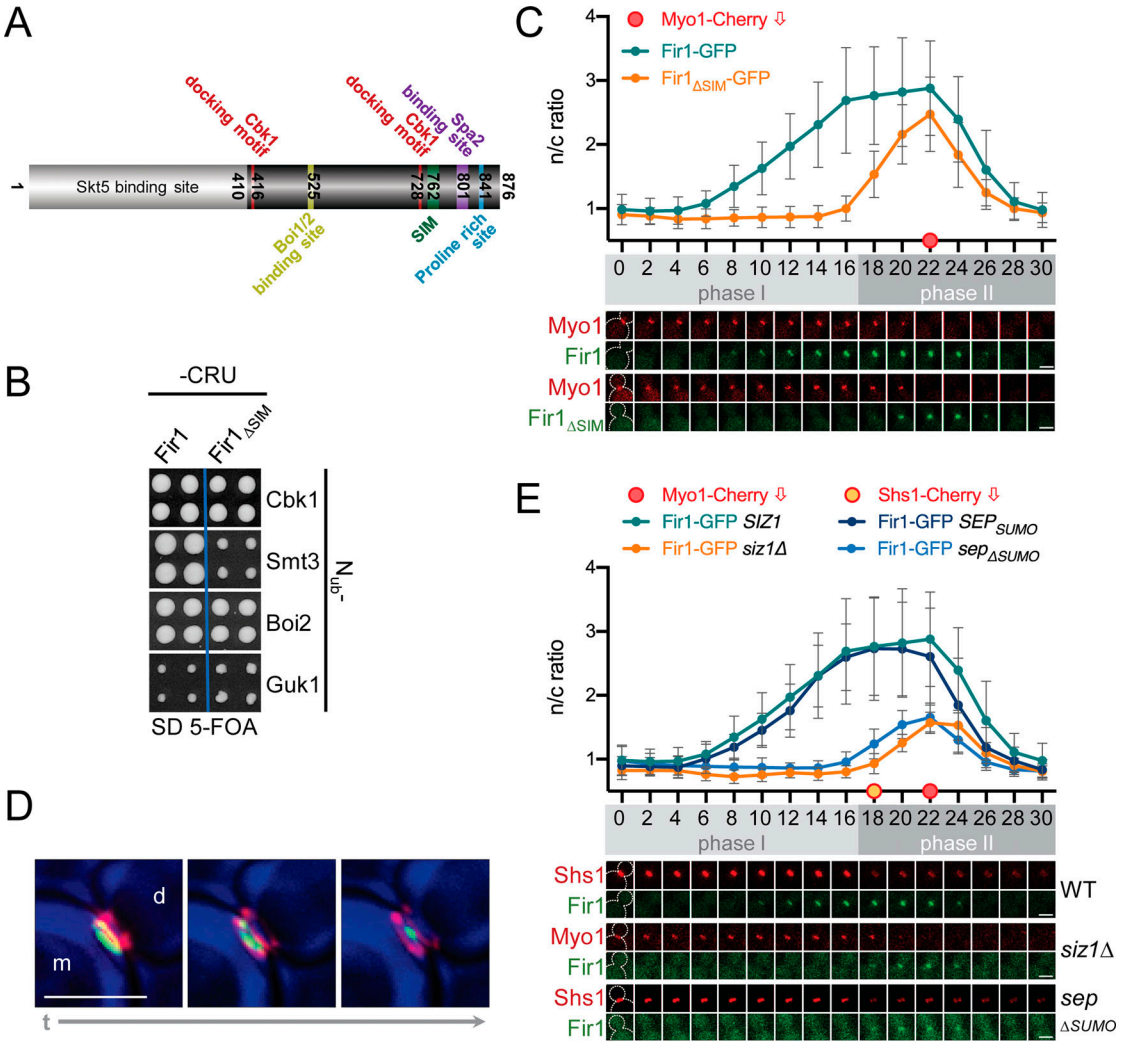

Figure 1. **Fir1 is recruited to the bud neck by the sumoylated septins. (A)** Cartoon of Fir1 indicating the known and herein discovered binding sites to other proteins. Amino acid positions bordering the motifs are indicated. **(B)** Cutouts of a Split-Ub array of diploid yeast cells expressing genomic Fir1CRU (CRU; C-terminal half of Ubiquitin [C_{ub}]-R-Ura3; left panel), $Fir1_{\Delta SIM}$CRU (right panel) together with the indicated N_{ub} fusions of known binding partners of Fir1, or the negative control N_{ub}-Guk1 (N_{ub}, N-terminal half of Ubiquitin). Four independent matings were arrayed as quadruplets on media containing 5-FOA. Colony growth indicates interaction between the fusion proteins. **(C)** Fluorescence intensities (upper panel) and stills of the bud necks of representative cells (lower panel) coexpressing Fir1-GFP (n = 29) or $Fir1_{\Delta SIM}$-GFP (n = 25) and Myo1-Cherry during cytokinesis. The ratio of bud neck fluorescence divided by cytosolic fluorescence (n/c ratio) is shown as mean ± standard deviation (SD). Images were taken every 2 min. The filled red circle (minute 22) indicates the time point of Myo1 disappearance. Phase I indicates association of Fir1 with the septin ring, phase II localization within the SSDR. **(D)** Deconvoluted images of Fir1-GFP associated with the Cherry-labeled septin ring (Shs1-Cherry) shortly before (left panel), during (middle panel), and shortly after ring splitting (right panel). m and d indicate mother and daughter cells, respectively. **(E)** As in C but with cells co-expressing Myo1-Cherry with Fir1-GFP in wild type (as reference from C) or *siz1*Δ cells (n = 22), or with cells coexpressing Shs1-Cherry and Fir1-GFP in wild type (n = 19, Fir1-GFP SEP_{SUMO}) or in $sep_{\Delta sumo}$ cells (n = 23, Fir1-GFP $sep_{\Delta SUMO}$). The orange-filled circle (time point 18) indicates the sudden decrease of the Shs1-Cherry signal. The significance of the differences between Fir1-GFP signal intensities of wild type and the deletion strains are shown in Fig. S1 C. Reintroducing a plasmid-encoded *SIZ1* into the *siz1*Δ cells restored the targeting of Fir1-GFP (Fig. S1 B). Error bars, SD. All scale bars = 3 µm.

the profile of $Fir1_{\Delta SIM}$ (Fig. 3, B and C). The simultaneous deletion of the potential Spa2-binding site and the SIM motif completely abolished phase I and nearly completely phase II targeting of $Fir1_{\Delta SIM\Delta 801-820}$-GFP (Fig. 3, B and C).

Testing different fragments of Spa2 in a Split-Ub interaction assay restricted the Fir1 binding site onto Spa2's C-terminal 192 residues (Fig. 3 D). A bacterially expressed GST fusion to $Fir1_{741-876}$ (GST-$Fir1_{741-876}$) precipitated the purified His-tagged C-terminal domain of Spa2 (His-$Spa2_{1,314\text{-end}}$; Fig. 3 F). We conclude that C-terminal domains of Fir1 and Spa2 form a stable complex that anchors Fir1 between the SSDR of dividing cells. Consequently, cells expressing Spa2 without its C-terminal domain ($spa2_{1-1,274}$) lacked phase II targeting of Fir1-GFP, while $Spa2_{1-1,274}$-GFP still binds indistinguishably to the bud neck (Fig. 3, E and C).

Fir1 is a bud neck receptor for Skt5 during cytokinesis

Fir1 might transfer across the septins to carry other proteins piggyback into the space between the SSDR. We measured the fluorescence intensities of GFP fusions to those Fir1 interaction

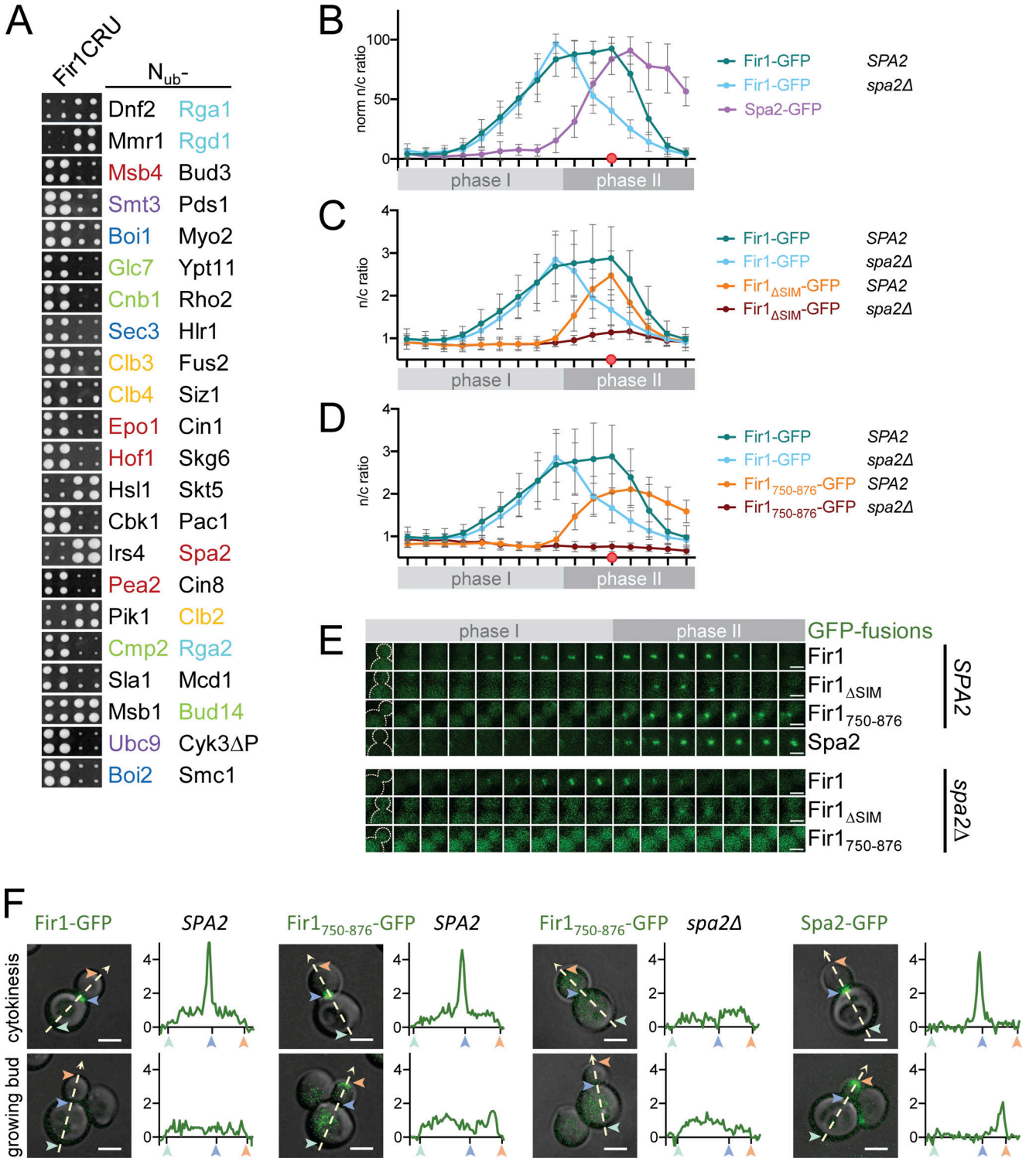

Figure 2. **Spa2 recruits Fir1 between the SSDR. (A)** Cutouts of a Split-Ub array of 540 diploid yeast cells each expressing genomic Fir1CRU together with a different N_{ub} fusion as in Fig. 1 B. Identities of the N_{ub} fusions are given next to the respective cutouts. Shared colors of the N_{ub} fusions indicate a common process. Red: polarisome; purple: SUMO conjugation; dark blue: exocytosis; light blue: Rho GAPs; yellow: mitotic cyclins; green: phosphatases and their adaptors. The complete analysis is shown in Fig. S2, and the complete list of binding partners in Table S1. **(B)** As in Fig. 1 C but with cells co-expressing Fir1-GFP with Myo1-Cherry in the presence (as reference from Fig. 1 C) and absence of Spa2 (n = 26), or coexpressing Myo1-Cherry with Spa2-GFP (n = 18). n/c ratios are shown. Reintroducing a plasmid-borne *SPA2* into the *spa2*Δ cells restored the targeting of Fir1-GFP (Fig. S3 B). **(C)** As in Fig. 1 C but with cells co-expressing Fir1-GFP (as reference from Fig. 1 C) or $Fir1_{\Delta SIM}$-GFP with Myo1-Cherry in the presence (as reference from Fig. 1 C) or absence (n = 23) of Spa2. **(D)** As in Fig. 1 C but with cells coexpressing $Fir1_{750-876}$-GFP with Myo1-Cherry in the presence (n = 22) and absence (n = 20) of Spa2. Fir1-GFP from Fig. 1 C and Fir1-GFP in *spa2*Δ from panel B are shown as references. The significance of the differences between Fir1-GFP and $Fir1_{750-876}$ in wild type and *spa2*Δ strains is shown in Fig. S3 D. **(E)** Stills of the bud necks of representative cells corresponding to the intensity profiles shown in B–D. **(F)** Fluorescence intensity profiles (shown in

arbitrary units) along the polarity axes of cells expressing, from left to right, Fir1-GFP, Fir1$_{750–876}$-GFP in the presence or absence of Spa2, or Spa2-GFP. Numbers and arrows correlate positions on the fluorescence intensity profiles with locations in the cells. Images in B–E were taken every 2 min. Error bars, SD. All scale bars = 3 µm.

partners that participate in cytokinesis or abscission and compared their profiles between wild type and *fir1*Δ cells (Fig. 2 A and Fig. 4). Deleting Fir1 did not affect the distributions of Bud14, Hof1, and Msb1 (Fig. S4 A). In contrast, the absence of *FIR1* reduced or abolished the phase I targeting of its binding partners Cbk1, Boi1, and Skt5 (Fig. 4, A–C and G; and Fig. S4, B and C; Brace et al., 2019; Grinhagens et al., 2020). While the amounts of Cbk1 and Boi1 recovered to wild type–like levels during phase II targeting, the concentration of Skt5 in the SSDR was significantly reduced (Fig. 4, A–C and Fig. S4 C). Contrary to the other

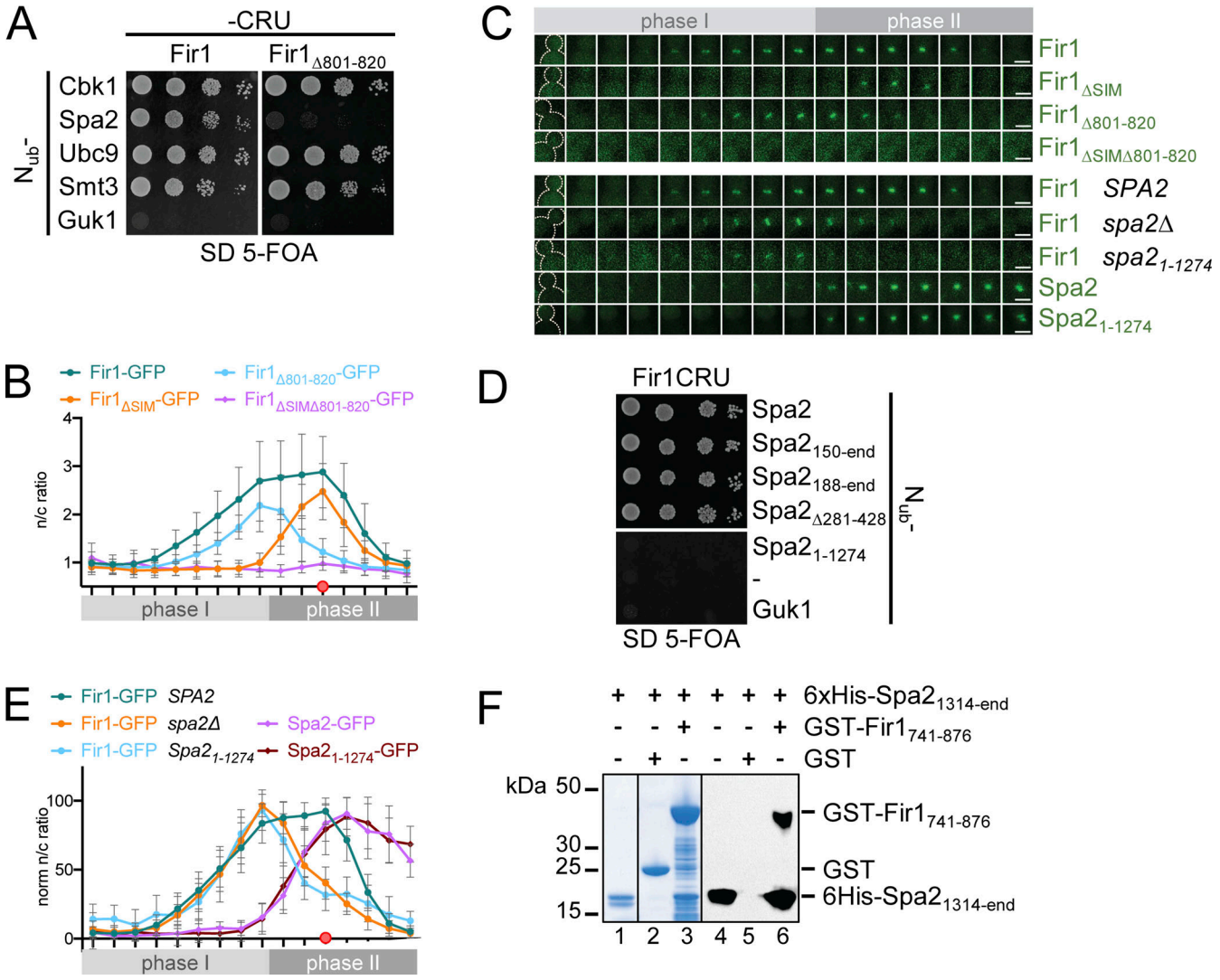

Figure 3. **Spa2 is the phase II receptor for Fir1. (A)** Split-Ub assay of cells coexpressing Fir1CRU (left panel) or Fir1$_{Δ801–820}$CRU (right panel) with N$_{ub}$ fusions to Spa2 and other binding partners of Fir1, or to Guk1 as negative control. Cells were grown to OD$_{600}$ = 1 and 4 µl, or 4 µl of a 10-fold serial dilution was spotted on media containing 5-FOA and selected for the presence of the N$_{ub}$ and C$_{ub}$ fusions. **(B)** As in Fig. 1 C but with cells expressing the GFP fusions to the indicated alleles of *FIR1* (Fir1$_{Δ801–820}$ *n* = 23; Fir$_{ΔSIMΔ801–820}$ *n* = 20; Fir1, Fir1$_{ΔSIM}$ as reference from Fig. 1 C). **(C)** Stills of the bud necks of cells corresponding to the intensity profiles shown in B and E. Scale bars = 3 µm. **(D)** Split-Ub assay as in A but with cells coexpressing Fir1CRU with the indicated N$_{ub}$ fusions to Spa2 and its mutants, or N$_{ub-}$ and N$_{ub}$-Guk1 as non-interacting controls. **(E)** As in Fig. 2 B but with cells coexpressing Myo1-Cherry with Fir1-GFP in *spa2*Δ (*n* = 18), or spa2$_{1–1,274}$ (*n* = 20) cells, and with wild-type cells coexpressing Myo1-Cherry and Spa2$_{1–1,274}$-GFP (*n* = 20). Fir1-GFP and Spa2-GFP as references from Fig. 1 C and Fig. 2 B. Images in B, C, and E were taken every 2 min. Error bars, SD. **(F)** Purified 6xHis-Spa$_{1,314-end}$ (lanes 1–6) was incubated with GST-Fir1$_{741–876}$ (lanes 3, 6) or GST-coupled beads (lanes 2, 5). Glutathione eluates were separated by SDS-PAGE and stained with Coomassie (lanes 1–3), or transferred onto nitrocellulose and stained with anti-His antibody (lanes 4–6). Detection of GST-Fir1$_{741–876}$ by the anti-His antibody (lane 6) indicates binding of nitrocellulose-detached 6xHis-Spa2$_{1,314-end}$ to nitrocellulose fixed GST-Fir1$_{741–876}$ (Fig. S3 E). Source data are available for this figure: SourceData F3.

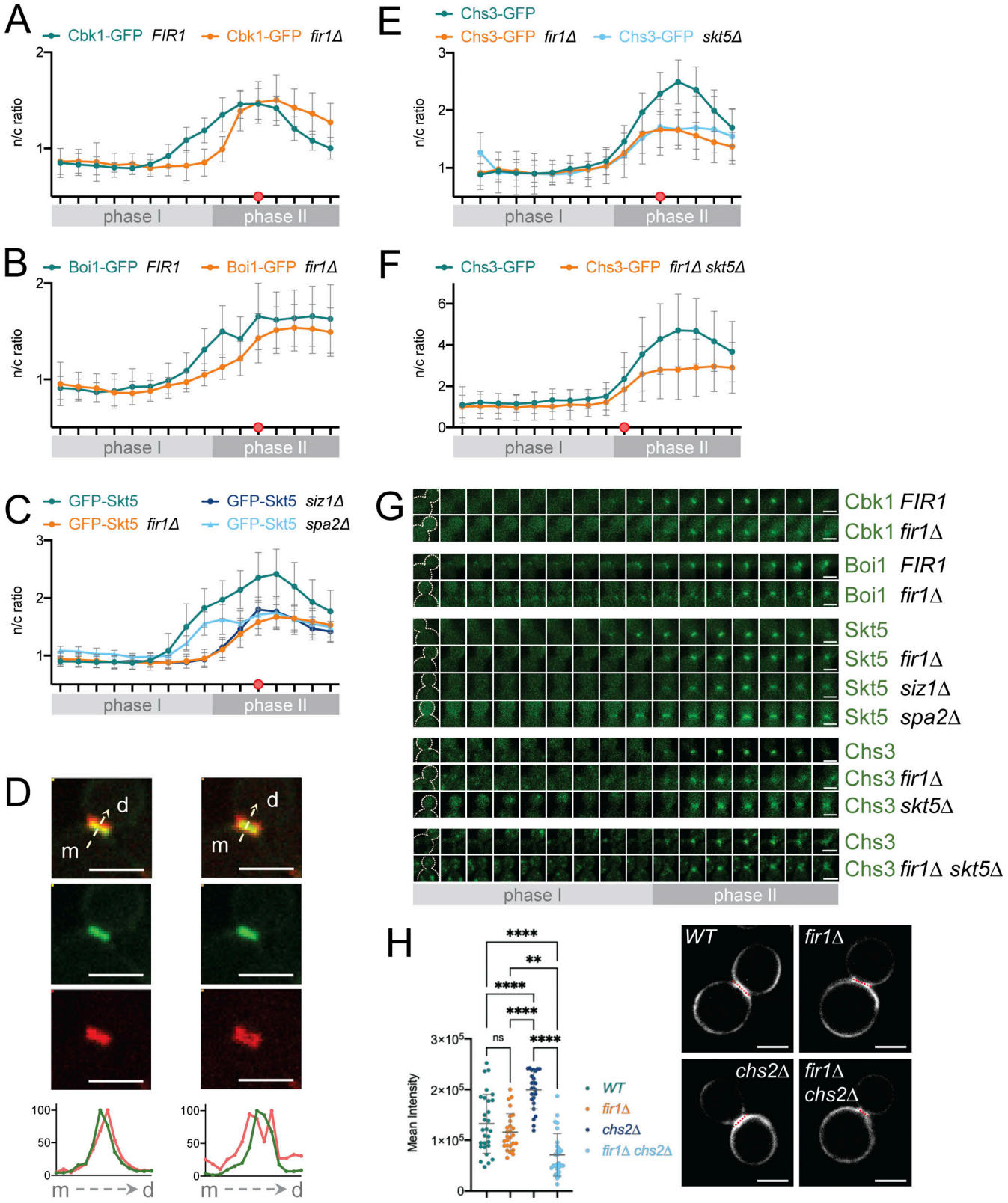

Figure 4. **Fir1 carries Skt5 between the SSDR. (A)** As in Fig. 1 C but with cells coexpressing Cbk1-GFP together with Myo1-Cherry in the presence (n = 20) or absence (n = 20) of *FIR1*. **(B)** As in Fig. 1 C but with cells coexpressing Boi1-GFP with Myo1-Cherry in the presence (n = 20) or absence (n = 25) of *FIR1*. **(C)** As in Fig. 1 C but with cells coexpressing Skt5-GFP with Myo1-Cherry in the presence (n = 22) or absence of *FIR1* (n = 27), in the absence of *SIZ1* (n = 23), or in the absence of *SPA2* (n = 21). **(D)** Images of GFP-Skt5 associated with the Shs1-mCherry–labeled septin ring shortly before (upper left panels from top to bottom: overlay, GFP-, Cherry-channel) and shortly after ring splitting (upper right panels from top to bottom: overlay, GFP, Cherry channel). m and d indicate mother and daughter cell, respectively. Lower panels: Intensity plots in relative fluorescent units of the GFP (green) and Cherry (red) channels along the arrows

orthogonal to the septin rings before (left panel) and after (right panel) septin ring splitting. **(E)** As in Fig. 1 C but with cells coexpressing Chs3-GFP with Myo1-Cherry in wild type (n = 20), in *fir1*Δ cells (n = 20), or in *skt5*Δ cells (n = 20). **(F)** As in Fig. 1 C but with cells co-expressing Chs3-GFP with Shs1-mCherry in wild type (n = 40) or in *fir1*Δ*skt5*Δ cells (n = 40). The significance of the differences between the profiles in B, C, E, and F are shown in Fig. S4, B–E. **(G)** Stills of the bud necks of cells corresponding to the intensity profiles shown in C, E, and F. Images were taken every 2 min. Scale bar = 3 µm. **(H)** Left panel: Mean fluorescence intensities of calcofluor-stained bud necks of wild-type (n = 29), *fir1*Δ (n = 27), *chs2*Δ (n = 25), and *chs2*Δ *fir1*Δ cells (n = 28). ****P < 0.0001; **P < 0.01; ns = not significant. Right panel: Representative stills of calcofluor-stained cells from each genotype. Error bars, SD. Scale bar = 3 µm.

interaction partners, Skt5 seems to require continuous binding to Fir1 for its two-step translocation into the SSDR.

Skt5 activates Chs3 and thus determines where and when chitin synthesis occurs (Ono et al., 2000; DeMarini et al., 1997). Recruited by the Bni4-Glc7 complex, Skt5 forms a ring around the incipient bud site and the neck of small budded cells (Larson et al., 2008; DeMarini et al., 1997; Kozubowski et al., 2003). It subsequently spreads out on the plasma membranes of mother and daughter cells before being concentrated independently of Bni1-Glc7 at the bud neck during mitosis (DeMarini et al., 1997; Gohlke et al., 2018; Kozubowski et al., 2003). Microscopy of GFP-Skt5 expressing yeast cells revealed that Skt5, similar to Fir1, contacted the septin ring first at the mother side before entering the space between the SSDR (Fig. 4 D). Inhibiting Smt3 modification of the septins in a *siz1*Δ strain abolished phase I targeting of Skt5 and decreased the amount of GFP-Skt5 between the SSDR during phase II targeting (Fig. 4, C and G; and Fig. S4 C). The deletion of *SPA2* did not influence the targeting of Skt5 to the septin hourglass but substantially reduced its amount between the SSDR (Fig. 4, C and G; and Fig. S4 C). These experiments confirm Fir1 as the mitosis-specific bud neck receptor for Skt5.

Fir1-Skt5 targets Chs3 to the SSDR and stimulates chitin synthesis during cytokinesis

Skt5 activates Chs3 at the bud neck of dividing cells (DeMarini et al., 1997; Kozubowski et al., 2003). The bud neck appearance of Chs3 coincides with the phase II targeting of the Fir1-Skt5 complex (Fig. 4 E; Okada et al., 2020). By comparing the fluorescence intensity profiles between wild type and *fir1*Δ cells, we could show that *fir1*Δ cells enriched significantly less Chs3-GFP at the bud neck than wild-type cells (Fig. 4, E and G; and Fig. S4 D). The deletion of Skt5 reduced the Chs3-GFP signal to a similar extent (Fig. 4, E and G; and Fig. S4 D). Chs3-GFP also stayed less focused within the space between the SSDR of *fir1*Δ and skt5Δ cells (Fig. 4 G). Deleting *SKT5* and *FIR1* in the same cell (*fir1*Δ *skt5*Δ) reduced the amount of CHs3-GFP at the bud neck to a similar extent as each single deletion (Fig. 4, F and G; and Fig. S4 E). We conclude that a complex containing Fir1 and Skt5 supports the targeting and/or anchorage of Chs3 during cellular abscission (Reyes et al., 2007).

A deletion of *FIR1* should consequently reduce the chitin levels in the secondary septum. Indeed, when we compared wild-type cells with *fir1*Δ cells, we observed a tendency for *fir1*Δ cells to produce less chitin in the septum. The effect was, however, not significant (Fig. 4 H). We reasoned that the chitin-rich primary septum might overshadow the influence of Fir1 on the secondary septum. To address this presumption, we compared the calcofluor staining of wild-type cells with cells lacking *CHS2* and cells lacking both *CHS2* and *FIR1*. *chs2*Δ cells displayed an increase in chitin deposition at the bud neck when compared with wild-type cells, whereas the deletion of Fir1 in *chs2*Δ cells (*fir1*Δ*chs2*Δ) resulted in a threefold reduction in chitin content when compared with *chs2*Δ cells (Fig. 4 H). We conclude that the Fir1-Skt5 complex stimulates the synthesis of chitin in the secondary septum of dividing cells.

Fir1 contains a separate binding site for Skt5

Skt5 is attached to the plasma membrane by a C-terminally coupled farnesyl moiety (Grabińska et al., 2007). Our findings suggest that Fir1 first links Skt5 to the septin hourglass before the complex relocates between the SSDR. This model implies that the interface of Fir1 for Skt5 should not overlap with those for Smt3 and Spa2. Indeed, Split-Ub interaction analysis of fragments of Fir1 localized the binding site for Skt5 to the supposedly disordered N-terminal 410 residues of the protein (Fig. 5 A and Fig. 1 A; Jumper et al., 2021). A GST fusion to the N-terminal region of Fir1 (GST-Fir1$_{1–410}$) precipitated the bacterial-expressed His-Skt5 and a fragment of Skt5 that harbored its central Sel1-like protein (SEL) domain (His-Skt5$_{146–550}$; Fig. 5 B and Fig. S5). The Fir1-Skt5 complex could also be reconstituted by incubating nitrocellulose membrane-tethered GST-Fir1$_{1–410}$ with *E. coli* extracts containing His-Skt5$_{146–550}$ (Fig. 5 C). We conclude that the interfaces of the Fir1-Skt5 complex are provided by the central SEL domain of Skt5 and the N-terminal half of Fir1.

Degradation of Fir1 resets the targeting of Skt5

Fir1 is a substrate of the Cdh1-activated ubiquitin ligase APC and becomes degraded at the end of cytokinesis (Ostapenko et al., 2012). Accordingly, deletion of Cdh1 raised the cytosolic levels of Fir1 and led to prominent tip staining of Fir1-GFP during bud growth (Fig. 6, A–C). Besides a strong cytosolic signal, the fluorescence intensity profile of Fir1-GFP in *cdh1*Δ cells showed phase I targeting and a stronger and longer enrichment between the SSDR (Fig. 6, A–C; Fig. S6 A). Deviating from Fir1, GFP-Skt5 lacked phase I targeting in *cdh1*Δ cells and showed a reduced enrichment between the SSDR (Fig. 6, B and D; and Fig. S6 B). We conclude that the degradation of Fir1 at the end of cytokinesis is required to properly reset the mechanism for Skt5 enrichment in the next cell cycle.

Discussion

Fir1 is the first identified sumoylation-dependent binding partner of the septins. In line with the kinetics of their sumoylation, Fir1 is recruited to the septins shortly before the visible onset of cytokinesis and is released as soon as the transition of the

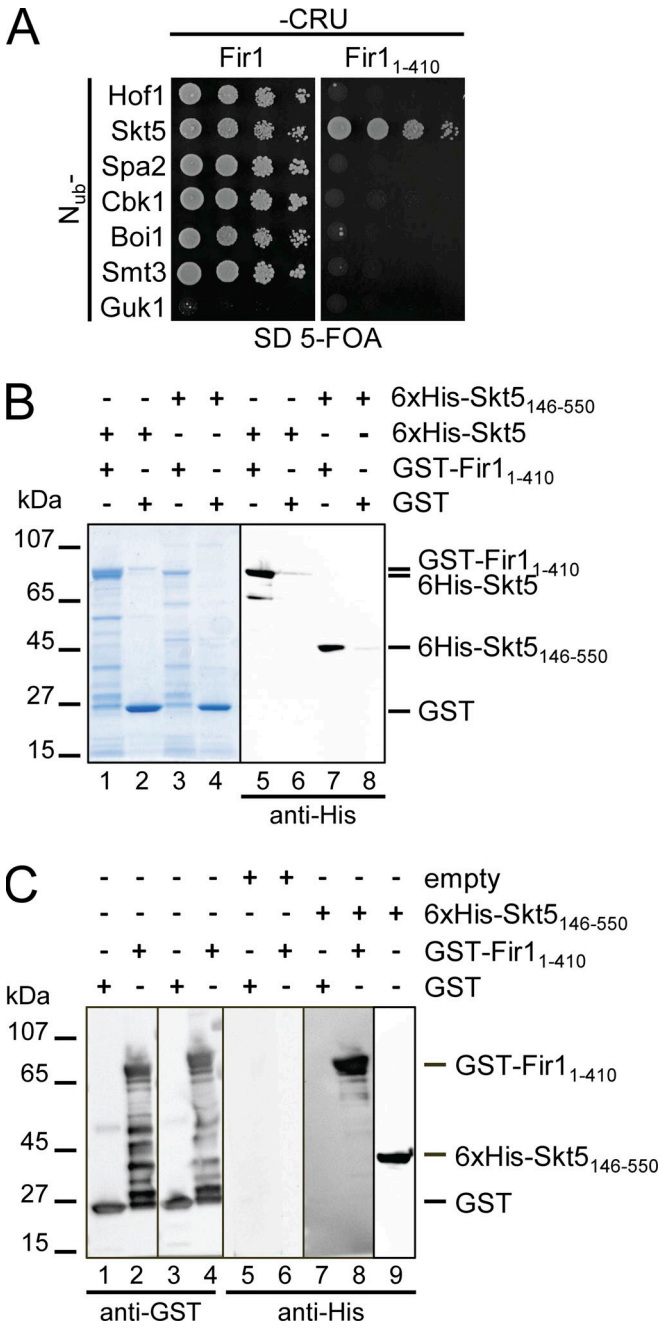

Figure 5. **Skt5 and Fir1 form a protein complex. (A)** Split-Ub assay as in Fig. 3 A but with cells coexpressing Fir1CRU (left panel) or $Fir1_{1–410}$CRU (right panel) with the indicated N_{ub} fusions of binding partners of Fir1, or N_{ub}-Guk1 as a negative control. **(B)** Extracts of *E. coli* expressing 6xHis-Skt5 (lanes 1, 2, 5, 6), or 6xHis-$Skt5_{146–550}$ (lanes 3, 4, 7, 8) were incubated with GST-$Fir1_{1–410–}$ (lane 1, 3, 5, 7), or GST-coupled beads (lanes 2, 4, 6, 8). Glutathione eluates were separated by SDS-PAGE and stained with Coomassie (lanes 1–4), or transferred onto nitrocellulose and stained with anti-His antibody (lanes 5–8). Input fractions are shown in Fig. S5. **(C)** Extracts of *E. coli* cells expressing GST-$Fir1_{1–410}$ (lanes 2, 4, 6, 8), GST (lanes1, 3, 5, 7), or 6xHis-$Skt5_{146–550}$ (lane 9) were separated by SDS-PAGE, transferred on nitrocellulose and either probed directly with anti-GST antibody (lanes 1–4), or anti-His antibody (lane 9), or incubated first with diluted extracts of *E. coli* cells expressing no additional protein (lanes 5, 6), or 6xHis-$Skt5_{146–550}$ (lanes 7, 8), before being incubated with anti-His antibody (lanes 5–8). Source data are available for this figure: SourceData F2.

hourglass to the SSDR occurs. The released Fir1 is retained at the bud neck by the perfectly scheduled appearance of its newly discovered binding partner Spa2. The chronology of the interactions moves Fir1 from the periphery of the septin hourglass to the center of the SSDR.

Intuitively, crossing the septin barrier should proceed in two steps: release from the desumoylated septins into the cytosol, followed by binding to the SSDR-located Spa2. However, Fir1's binding partner Skt5 is attached to the membrane and might prevent the complex from freely entering the cytosol after septin desumoylation (Meissner et al., 2010; Larson et al., 2008; Reyes et al., 2007). Interestingly, GFP-Skt5 and Fir1-GFP have not been observed within endosomal compartments during cytokinesis. This observation, coupled with the finding that septin sumoylation enhances the formation of the Fir1-Skt5 complex within the SSDR, leads us to propose that the Fir1-Skt5 complex traverses the septin barrier directly.

In the initial step of this novel and still hypothetical targeting mechanism, septin sumoylation recruits Skt5 to the periphery of the septin hourglass. As the hourglass transforms into a double ring, a brief opening in the septin gate allows the Fir1-Skt5 complexes to move along their concentration gradient via directed diffusion into the space between the SSDR. Gradual desumoylation, catalyzed by Ulp1 from the maternal side of the ring, prevents backward movement. Meanwhile, Spa2 effectively entraps the incoming Fir1-Skt5 complexes within the double ring (Fig. 6 E).

It is important to note that our hypothesis lacks an independent experimental validation for its central assumption that the septins become more permeable to membrane-associated proteins during the hourglass-SSDR transition (Dobbelaere and Barral, 2004; Wloka et al., 2011). However, it is known from different experimental approaches that the majority of septin filaments disappear during this transition. The remaining septin units exhibit increased mobility and temporarily lose their uniform orientation (DeMay et al., 2011; Dobbelaere et al., 2003; Ong et al., 2014). One of the proposed models to explain this behavior posits the depolymerization of paired filaments, followed by their repolymerization into circumferential filaments (DeMay et al., 2011; Ewers, 2011). In this manner, the transiently dynamic state of the septins might indeed facilitate the movement of Fir1-Skt5 complexes across the forming ring.

Such a permeable septin gate should already allow a significant fraction of Skt5 to passively diffuse into the SSDR without Fir1. Incoming interaction partners like Chs3 or Hof1 might then trap the protein between the SSDR (Oh et al., 2017; DeMarini et al., 1997; Reyes et al., 2007). In agreement with this prediction, we observed that the loss of sumoylated septins, or the deletion of either Fir1 or Spa2, did not completely prevent Skt5 from accumulating between the SSDR (Fig. 4 C). This Fir1-independent enrichment at the bud neck could also explain why Fir1-, $Fir1_{\Delta SIM}$-, or $Fir1_{\Delta 801–820}$-GFP, all retaining their Skt5 binding site, still show some residual accumulation between the SSDR of *spa2*Δ cells, whereas $Fir1_{750–876}$-GFP does not (Figs. 2 and 3).

We observed that the absence of sumoylation seems to affect the accumulation of Fir1 between the SSDR more severely than the loss of the Smt3-binding site in $Fir1_{\Delta SIM}$ (Fig. 1, C and E). This

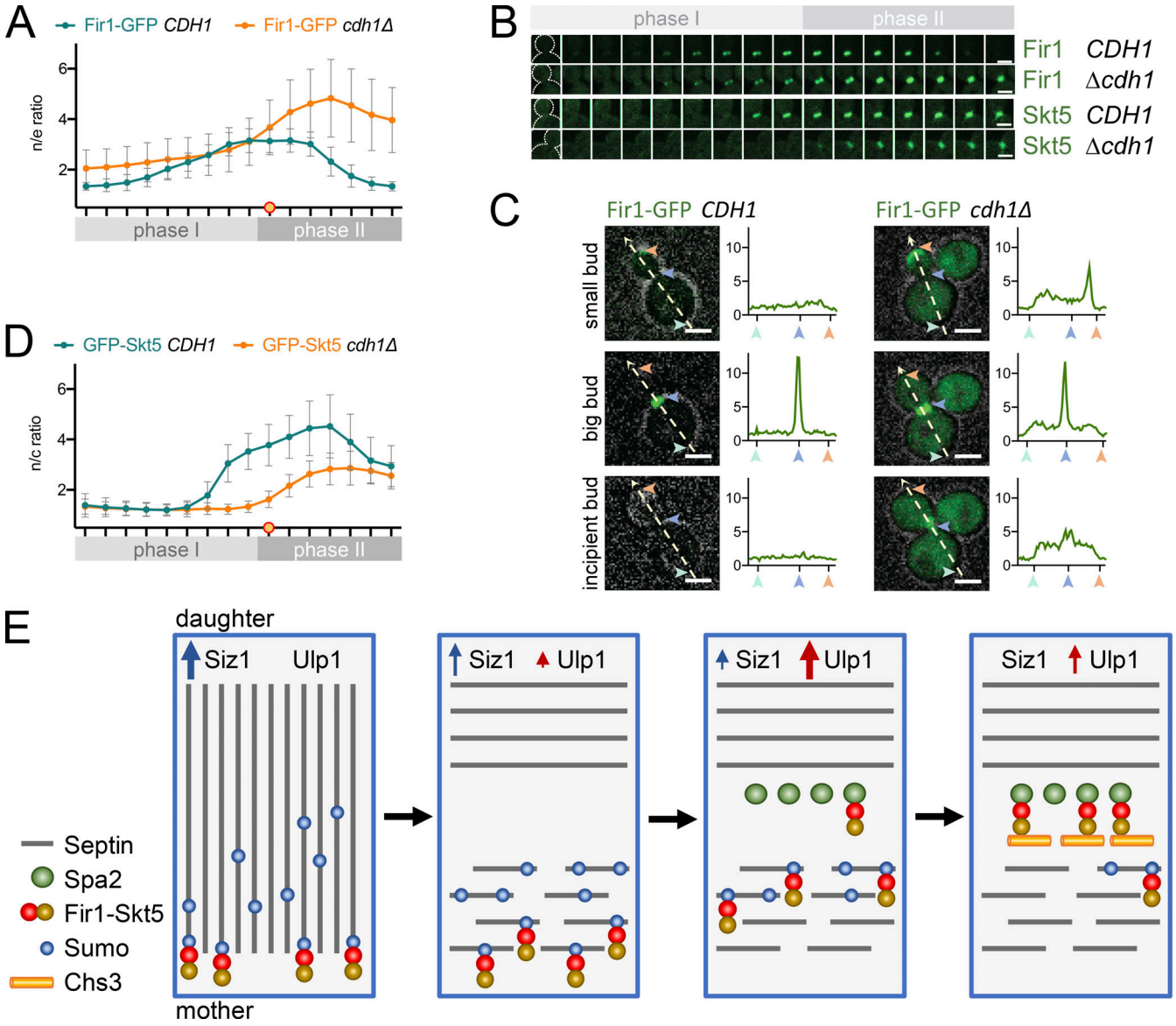

Figure 6. **Fir1 degradation resets the bud neck targeting of Skt5. (A)** As in Fig. 1 C but with cells coexpressing Fir1-GFP together with Shs1-Cherry in the presence (n = 24) or absence of *CDH1* (n = 25). The fluorescence intensities are shown as a ratio to extracellular background (n/e; see Materials and methods). **(B)** Stills of the bud necks of cells corresponding to the intensity profiles shown in A and D. **(C)** Fir1-GFP fluorescence intensity profiles (arbitrary fluorescent units) along the polarity axis in a wild type (left panels) and a *cdh1*Δ cell (right panels). Shown from top to bottom: S phase, cytokinesis, G1 phase. Numbers and arrows correlate positions on the fluorescence intensity profiles with locations in the cells. **(D)** As in A but with cells coexpressing GFP-Skt5 and Shs1-Cherry in the presence (n = 23) or absence (n = 25) of *CDH1*. The orange-filled circle indicates splitting of the septin ring in A and D. The significance of the differences between the profiles A and D are shown in Fig. S6, A and B. Images in A, B, and D were taken every 2 min. Error bars, SD. Scale bars = 3 µm. **(E)** A model of how the Fir1-Skt5 complex might transfer into the SSDR. From left to right: Sumoylation at the mother side of the intact septin hourglass concentrates the membrane-bound Fir1-Skt5 complex at the edge of the hourglass. The transformation into the split septin rings reduces the number and length of the septin filaments and switches the direction of the remaining filaments perpendicular to the mother–daughter axis (only shown for the mother side). This process creates temporal holes within the septin grid (only shown for the mother side). Fir1-Skt5 diffuses through the temporal holes of the septin grid along the unoccupied Smt3 sites. The Spa2 trap within the split septin rings and the gradual desumoylation direct the diffusion of the Fir1-Skt5 complex into the space between the SSDR. The holes are filled by repolymerization and Chs3 is captured and activated by the Skt5-Fir1-Spa2 complex.

finding might point to an additional role for septin sumoylation on the state of the septins during the hourglass-ring transitions or its properties as a diffusion barrier. These features might facilitate the transfer of Fir1 independently of its SIM and might correspond with findings in mammalian cells, where sumoylation was shown to alter the bundling properties of the septins during cytokinesis (Ribet et al., 2017).

Like other proteins involved in cytokinesis, Fir1 undergoes degradation by the Cdh1-activated APC at the conclusion of the cell cycle (Ostapenko et al., 2012; Tully et al., 2009). Disruption of this degradation results in the accumulation of Fir1 in the cytosol, yet does not affect its targeting during phases I and II. Surprisingly, in *cdh1*Δ cells, Skt5 was no longer recruited during phase I targeting. This surplus of Fir1 may potentially compete

with the Fir1-Skt5 complex for the limited pool of sumoylated septins. Consequently, less Skt5 is recruited to the septins and subsequently enriched between the SSDR. However, alternative explanations remain plausible. This includes the potential presence of an inhibitor that disrupts the formation of the Fir1-Skt5 complex during the final stages of cytokinesis, which subsequently undergoes degradation by Cdh1 in the ensuing G1 phase.

The absence of Fir1 leads to a reduction in chitin content within the secondary septum. This decline in chitin content closely corresponds to the diminished presence of Skt5 and Chs3 at the bud neck of cells lacking Fir1. Consequently, our research has identified Fir1 as the bud neck receptor for Skt5, the pivotal activator of Chs3. Our finding suggests that the unique targeting of Fir1-Skt5 to the bud neck may be a result of the need to prevent premature activation of Chs3 during its conventional transport to the plasma membrane.

Fir1 has recently emerged as a central player in a novel checkpoint mechanism, ensuring that cell separation proceeds only after the successful completion of preceding steps (Brace et al., 2019). This checkpoint can be artificially activated by the deletion of Chs2 or proteins like Cyk3 or Inn1, which promote chitin synthesis in the primary septum (Brace et al., 2019; Foltman et al., 2016; Devrekanli et al., 2012). To compensate for reduced primary septum formation, there is an increased production of Chs3 and Fks1 at the cell division plane (Okada et al., 2020). The deletion of Fir1 exacerbates the growth impairment of these cells and results in a significantly thinner secondary septum (Brace et al., 2019). According to Brace et al., this deletion of Fir1 appears to trigger premature secretion of the Chitinase Cts1, consequently reducing chitin levels in the primary septum.

Our study introduces a novel role for Fir1 by demonstrating that, as part of the Fir1-Skt5 complex, it also stimulates chitin synthesis during cytokinesis. Thus, Fir1 appears to respond to primary septum synthesis defects through two distinct mechanisms: by inhibiting the degradation of the primary septum and, concurrently, promoting chitin synthesis for the secondary septum.

Materials and methods

Growth conditions, cultivation of yeast strains, and genetic methods

All yeast strains were derivatives of JD47, a segregant from a cross of the strains YPH500 and BBY45, and are listed in Table S2 (Dohmen et al., 1995). Yeast strains were cultivated in synthetic defined (SD) or yeast extract peptone dextrose (YPD) media at the indicated temperatures. Media preparation followed standard protocols (Glomb et al., 2020). SD medium for Split-Ub assays contained in addition 1 mg/ml 5-fluoro-orotic acid (5-FOA; Formedium). Gene deletions and promoter replacements by P_{MET17} were performed by homologous integration of the cassettes derived by PCR from the plasmids pFA6a-hphNT1, pFA6a- natNT2, pFA6a-kanMX6, pFA6a-CmLEU2, or pYM-N35 (Bähler et al., 1998; Janke et al., 2004). *E. coli* XL1 blue cells were used for plasmid amplification and grown at 37°C in lysogeny broth (LB) medium containing antibiotics. *E. coli* BL21 cells were used for protein production and were grown in LB or super broth (SB) medium at 37°C.

Generation of plasmids and yeast strains

Detailed lists of all plasmids used in this study are provided in Table S3. Genomic gene fusions were obtained as described (Wittke et al., 1999; Neller et al., 2015; Dünkler et al., 2012). In brief, fusions of *GFP*, *mCHERRY*, or *CRU* to *SPA2*, *MSB1*, *CBK1*, *HOF1*, *BUD14*, *CHS3*, *BOI1*, *SHS1*, *MYO1*, and in some cases to *FIR1*, were constructed by PCR amplification of the respective C-terminal ORFs without stop codon from genomic DNA. The obtained DNA fragments were cloned via *Eag*I and *Sal*I restriction sites in front of the *CRU*, *GFP*, *mCherry* module on a pRS303, pRS304, or pRS306 vector (Wittke et al., 1999). The plasmids were linearized using a single restriction site within the C-terminal genomic DNA sequence and transformed into yeast. Successful integration was verified by PCR of single yeast colonies with diagnostic primer combinations using a forward primer annealing in the target ORF but upstream of the linearization site, and a reverse primer annealing in the C-terminal module. Most *Fir1* fusions were created by introducing a PCR fragment carrying GFP and an *TRP1* selection cassette flanked by 45 bp homologous to the 3′-end of the *FIR1* ORF and the 5′-end of its 3′ non-translated region, respectively. GFP-*SKT5* was generated via CRISPR/Cas9-mediated insertion of a PCR fragment encoding GFP flanked by 45 bp homologous to the region upstream of the start codon of *SKT5* and the 5′-end of its ORF. Deletions and base exchanges in the genomic copies of *FIR1* and *SPA2* were achieved by CRISPR/Cas9 manipulation using plasmid pML104 or pML107 containing specific 20mer guide RNA sequences, and template oligonucleotides for exchanging the information on the genomic DNA (Table S4; Laughery et al., 2015). The correct insertions of PCR fragments and mutations were verified by PCR amplification and sequencing. Gene deletions were obtained by replacing the ORF through single-step homologous recombination with an antibiotic resistance cassette derived by PCR from the plasmids pFA6a-hphNT1, pFA6a-natNT2, pFA6a-kanMX6, pFA6a-CmLEU2, or pYM-N35 (Bähler et al., 1998; Janke et al., 2004).

Fragments of *FIR1*, *SPA2*, or *SKT5* were expressed as GST or 6xHis fusions in *E. coli* strains BL21 or BL21 Gold. Fragments for the GST fusions were amplified from yeast genomic DNA using primers containing *Bam*HI/*Eco*RI restriction sites. The PCR products were fused in-frame behind GST on a pGex2T vector (GE Healthcare). 6xHis-tagged fragments were amplified from yeast genomic DNA using primers containing *Sfi*I restriction sites. The products were inserted into the pES plasmid, downstream and in-frame of a 6xHis-tag.

In vivo Split-Ub interaction analysis

Large-scale Split-Ub assays were performed as described (Dünkler et al., 2012). A library of 540 different α-strains, each expressing a different N_{ub} fusion, was mated with a P_{MET17}*FIR1*-CRU–expressing a-strain. Diploids were transferred as independent quadruplets on SD media lacking methionine and containing 1 mg/ml 5-FOA, and different concentrations of

copper sulfate to adjust the expression of the N_{ub} fusions. For small-scale interaction analysis, a- and α-strains expressing N_{ub} or C_{ub} fusion constructs were mated. The diploid cells were spotted onto SD-FOA medium in four 10-fold serial dilutions starting from OD_{600} = 1. Growth was recorded at 30°C every day for 2–5 d.

In vitro binding assays

E. coli *extracts*

An overnight culture of Hisx6-Spa2$_{1,314\text{-end}}$– or GST-Fir1$_{1–410}$–expressing *E. coli* BL21 Gold (GE Healthcare) was diluted into 500 ml of SB medium and incubated at 37°C to an OD_{600} of 0.8. The cultures were chilled to 18°C and incubated overnight at 18°C in the presence of 1 mM IPTG. Cells were centrifuged at 5,000 × *g* for 10 min, resuspended in PBS, and centrifuged at 4,000 × *g* for 10 min. The cell pellet was stored at −80°C. BL21 strains expressing GST-Fir1$_{741–876}$, 6xHis-SKT5, or 6xHis6-Skt5$_{146–550}$ were treated as above except that protein expression occurred in SB/1 mM IPTG for 4 h at 37°C.

The cell pellets were washed once in PBS and resuspended in 5 ml PBS containing protease inhibitor cocktail (Roche Diagnostics) and 1 mg/ml lysozyme. After 45 min on ice, cells were lysed by 3 × 2 min sonication with a Bandelin Sonapuls HD 2070 (Reichmann Industrieservice). Extracts were clarified by centrifugation at 40,000 *g* for 10 min at 4°C. 6xHis-Spa2$_{1,314\text{-end}}$–expressing strain BL21 was lysed in IMAC Buffer A (50 mM KH_2PO_4, pH 8.0, 300 mM NaCl, 20 mM imidazole) by lysozyme treatment and sonication, followed by IMAC purification on an Äkta purifier chromatography system using a 5 ml HisTrap Excel column (GE Healthcare). The column was washed by a linear imidazole gradient (20–70 mM), followed by elution in 200 mM imidazole. Eluted proteins were subsequently transferred on a PD10 column into PBS and concentrated. Enriched 6xHis-Spa2$_{1,314\text{-end}}$ was finally loaded onto a gel-filtration column (HiLoad 16/600 Superdex 200 pg) equilibrated in 20 mM 2-(N-Morpholino)ethansulfonsäure, 100 mM NaCl, pH 6.7. Peak fractions were pooled and used for the experiments.

Binding assay

All incubation steps were carried out under rotation at 4°C. GST or GST-tagged proteins were immobilized from *E. coli* extracts on 100 µl Glutathione–Sepharose beads in PBS (GE Healthcare). After incubation for 1 h at 4°C, with either *E. coli* extracts or purified proteins, the beads were washed three times, the bound material was eluted with GST elution buffer (50 mM Tris, 20 mM reduced glutathione), and subjected to SDS-PAGE followed by Coomassie Blue staining and western blot analysis using anti-His (H1029), or anti-GST (G1160) antibodies (Sigma-Aldrich).

Far-western blot

Enriched GST and GST-Fir1$_{1–410}$ were transferred onto nitrocellulose after SDS-PAGE. The membrane was blocked for 1 h in 20mM Tris, 150 NaCl, 0.1% Tween 20 (TBST) 2% milk powder (wt/vol), washed for 5 min in 10 ml TBST, and incubated for 1 h at 4°C with extracts (20-fold diluted in TBST) from *E. coli* expressing no additional protein or 6xHis-Skt5$_{146–550}$. After washing three times for 5 min with 10 ml TBST, the membrane was sequentially incubated at room temperature for 1 h with anti-His (H1029) and conjugated anti-mouse antibodies (A4416; Sigma-Aldrich; Wu et al., 2007).

Fluorescence microscopy

Microscopic observations were performed with two different fluorescence microscopes. The Axio Observer spinning disc confocal microscope (Zeiss) is equipped with an Evolve512 electron-multiplying charge-coupled device camera (Photometrics), a Plan-Apochromat 63×/1.4 oil differential interference contrast (DIC) objective, and a 100×/1.4 oil DIC objective. Fluorescence was excited with 488- and 561-nm diode lasers (Zeiss) and detected with high-efficiency filter sets 38 (GFP) and 45 (Cherry), respectively. Time-lapse experiments were carried out at 30°C in a PeCon Incubator controlled by a PeCon TempModule S1. Operations were performed with the ZEN2.6 (2012) software package (Zeiss).

The DeltaVision system (GE Healthcare) is provided with an IX71 microscope (Olympus), a 100× UPlanSApo 100 × 1.4 oil ∞/0.17/FN26.5 objective (Olympus), a steady-state heating chamber (Weather station by Prescision Control), and a Photofluor LM-75 halogen lamp. The standard live cell filter set (eGFP: excitation 470/40, emission 525/5; dsRed: excitation 580/20, emission 630/60) was used for fluorescence microscopy and images were recorded with either the Cascade II 512 electron-multiplying charge-coupled device camera (Photometrics) or the CoolSNAP HQ^2 High-Speed CCD camera (Photometrics). All operations were performed with the SoftWoRx 6.1.3. software (GE Healthcare).

For all microscopic analyses, yeast cultures were grown overnight in SD medium, diluted in 3–4 ml fresh SD medium, and grown for 2–3 h at 30°C to mid-log phase. Exposure times were adapted to the respective GFP- and mCherry-labeled proteins to reduce bleaching and phototoxicity.

Standard time-lapse experiments with the ZEISS microscope were carried out with the 63× objective in a Sarstedt 1-well on cover glass II incubation chamber. 100 µl culture was pipetted onto the glass bottom of the chamber and covered with a slice of standard solid SD medium. Images were taken in intervals of 2 min and obtained with a series of seven z-slices and a distance of 0.5 µm between adjacent z-slices.

Standard time-lapse experiments at the DeltaVision microscope were performed with the 100× objective and the Cascade II 512 camera. 1 ml mid-log phase cell culture was carefully pelleted and resuspended in 50 µl medium. 3 µl of this suspension was transferred on custom-designed glass slides containing solid SD medium with 1.8% agarose and immobilized with a coverslip. Images were taken in intervals of 2 min and obtained with a series of seven z-slices and a distance of 0.5 µm between adjacent z-slices.

Analysis of microscopic data

Image analysis and signal quantifications were carried out with the open source software platforms Image J for the data obtained with the DeltaVision microscope or Fiji for the data obtained with the ZEISS microscope (Schneider et al., 2012; Schindelin et al., 2012).

Quantitative evaluation of time-lapse experiments

For the quantification of bud neck signals in time-lapse series of cells undergoing cytokinesis, we generally employed yeast strains expressing two different fusion proteins. The protein of interest was translationally fused to GFP while mCherry fusions of either Shs1 or Myo1 served as marker proteins for the onset of cytokinesis. Sum projections of all relevant Z planes in both channels served as basis for all measurements. If not noted differently, circular regions of interest (ROI) of exactly 8 pixels in diameter were selected covering the bud neck region (1, bud neck signal), a region without obvious signal within either the daughter or mother cytosol (2, cytosolic signal), and an area outside the cell (3, background). The mean gray value of ROI 1–3 in both channels at 19 time points covering the period of cytokinesis was measured. Data analysis was carried out with Microsoft Excel (Microsoft Excel for Mac, version 16.66.1) and GraphPad Prism (Prism 9 for MacOS, version 9.0.2). The background (3) was subtracted from values (1) and (2) in both channels at every time point and the resultant values (s1) were divided by the cytosolic readings (s2) to obtain the ratio of bud neck to cytosol signal for both channels at each time point (n/c ratio, neck-to-cytosol ratio). The Shs1-Cherry signal drops dramatically when the septin ring splits (defined as minute 18 in this study) while Myo1-Cherry contracts and disappears rapidly at minute 22. To facilitate temporal alignment of the readings originating from different cells, each individual time series was normalized, meaning that the lowest value within each individual series was defined as 0% and the maximum value as 100% (normalized [norm] n/c ratio). The norm n/c ratio values obtained for the Cherry channel were plotted against time and utilized for a visual temporal alignment (facilitated by the loss/drop of the Myo1-/Shs1-Cherry signal) of the individual curves of this experiment. For each experiment, the n/c ratio as well as the norm n/c ratio series were aligned accordingly, and the averages and standard deviations of each time point in the GFP as well as the Cherry channel were determined. Normalization reduces the quantitative deviation between individual curves, facilitates alignment, and is useful for illustrating the relative timing of signals of comparable intensities. In most cases, we preferred to show the n/c ratio as this data set provides additional information on relative signal strength. We are aware that absolute fluorescence signal intensities vary considerably between experiments. The shown quantitative differences could be reproduced repeatedly and independently and represent the visual impression of the pictures very accurately.

Statistical evaluation

For all experiments where the curves of collated protein variants or genotypes displayed reproducibly deviating n/c ratio values, the statistical significance of the difference at selected time points was determined in GraphPad Prism. Kruskal–Wallis ANOVA tests were used for multiple comparisons, whereas Mann–Whitney tests were employed for the comparison of two data sets.

Images time series

For the illustration of bud neck signals, representative cells of the standard time-lapse experiments were chosen and max Z-projections were created in ImageJ or Fiji. Brightness and contrast settings of the GFP and Cherry channels were manually adjusted.

Specifications of selected microscopic experiments

Fig. 1 D and Fig. S1 A: The pictures in Fig. 1 D were obtained with the Deltavision microscope utilizing the 100× objective and the CoolSNAP HQ^2 camera. In a short time-lapse experiment, 20 Z-sections at 0.2-µm spacing were taken every 2 min. Images of the GFP and Cherry channels were deconvoluted with the softWoRx 6.1.3 software and subsequently 3D projected in ImageJ. Fig. 2 F: Images shown in Fig. 2 F originated from standard Deltavision time-lapse experiments. A max projection of the GFP channel was superimposed on single Z-sections of the bright field channel. Profiles were measured in single Z-sections of the same cells. A linear ROI with a width of 1 pixel was drawn centrally through budding cells from the mother to the daughter starting and ending outside the cells. The average of the extracellular values of the GFP channel was subtracted from each data point. The value for each data point was divided by the average of the extracellular values of the GFP channel. Fig. 4 D: The images of the bud neck in Fig. 4 D were obtained from a single cell at two different time points with the 100× objective at the Zeiss microscope. Overlays of sum projections of the GFP and Cherry channels are shown. The corresponding profiles were measured in single Z-sections of the same cell. A short linear ROI with a width of 1 pixel was drawn centrally through the bud neck from the mother to the daughter cell. The measurements of both channels were normalized. Fig. 4, E and F: Due to the patchy cytosolic distribution of Chs3-GFP, a circular selection of 13 pixels diameter in the mother cell was used as intracellular reference. Fig. 6 A: Due to the high level of cytosolic Fir1-GFP signal in cdh1Δ cells, the standard procedure for quantitative time-lapse analyses led to an underestimation of the bud neck signal. We thus decided to divide the measured bud neck signal by the reference value obtained outside the cell in wild type and *cdh1Δ* rather than a cytosolic reference point (n/e ratio, neck to extracellular ratio). Fig. 6 C: Images originate from standard Zeiss time-lapse experiments. A sum projection of the GFP channel was superimposed on a single Z-section of the bright field channel. Profiles were measured in single Z-sections of the same cells. A linear ROI with a width of 1 pixel was drawn centrally from the mother to the daughter starting and ending outside the cells. The value for each data point was divided by the average of the extracellular values of the GFP channel.

Quantitative calcofluor assay

500 µl of a logarithmically grown culture was centrifuged at 8,000 rpm for 3 min, resuspended in 100 µl of medium plus 1 µl of calcofluor White (20 µg/ml), and incubated at room temperature in the dark for 15 min. Cells were washed two times with 1× PBS and incubated for 15 min in the dark with 3.7% formaldehyde. Cells were again washed two times with 1× PBS, resuspended in 100 µl of PBS, and finally used for microscopy. Images were acquired on a Leica TCS SP8 confocal microscope equipped with 40× NA 1.3 oil objective. Fluorescence was excited

with a 405-nm diode laser (Leica) and detected spectrally using a HyD detector for a linear signal response. To quantify the amount of chitin at the bud neck of dividing cells, the fluorescence signal was measured along a line (open-source software Fiji, freehand tool, line width 3) across the bud neck. Data analysis was carried out with Microsoft Excel (Microsoft Excel for Mac, version 16.66.1) and GraphPad Prism (Prism 9 for MacOS, version 9.0.2). The statistical significance of the differences between the mean fluorescence intensities of the different strains was determined by one-way ANOVA tests.

Online supplemental material

Fig. S1 shows deconvoluted images of the bud neck of cells expressing Fir1-GFP and Fir1$_{\Delta SIM}$-GFP, the complementation of *siz1*Δ cells, and the statistical evaluation of the fluorescence intensity profiles of Fig. 1 E. Fig. S2 shows the Split-Ub interaction array. Fig. S3 shows the fluorescence intensity profiles of Spa2-GFP in different genetic backgrounds, the complementation of *spa2*Δ cells, the statistical evaluation of the fluorescence intensity profiles of Fig. 2 D, and the far-western analysis of Fir1$_{750–876}$ probed with Spa2$_{1,324\text{-end}}$. Fig. S4 shows the fluorescence intensity profiles of different bud neck localized proteins in the presence and absence of *FIR1* and the statistical evaluation of the fluorescence intensity profiles of Figs. 4, B, C, E, and F. Fig. S5 shows the input fractions of Fig. 5 B. Fig. S6 shows the statistical evaluation of the fluorescence intensity profiles of Fig. 6, A and D. Table S1 lists the Split-Ub discovered interaction partners of Fir1. Tables S2, S3, and S4 list the yeast strains, constructs, and primers used and created in this study.

Data availability

All strains and plasmids are available upon request. Image files of the time-lapse analysis, values of the measured fluorescence intensities, and the calculated ratios are accessible under the DOI 10.5281/zenodo.8405825 through the open-access repository Zenodo.

Acknowledgments

We thank N. Schmid and S. Timmermann for technical assistance. We thank J. Dohmen (University of Cologne, Cologne, Germany) for yeast strains, plasmids, and advice. We thank Dr. Christian Bökel of the Core Facility for Confocal and Multiphoton Microscopy of Ulm University for his support.

The work was funded by grants from the Deutsche Forschungsgemeinschaft to N. Johnsson (Jo 187/8-1).

Author contributions: Conceptualization: N. Johnsson. Investigation: J. Müller, M. Furlan, B. Grupp, and D. Settele. Writing - original draft: N. Johnsson; Writing - review & editing: N. Johnsson, J. Müller, and M. Furlan. Supervision: N. Johnsson and J. Müller. Funding acquisition: N. Johnsson.

Disclosures: The authors declare no competing interests exist.

Submitted: 6 January 2023
Revised: 5 October 2023
Accepted: 17 October 2023

References

Bähler, J., J.Q. Wu, M.S. Longtine, N.G. Shah, A. McKenzie III, A.B. Steever, A. Wach, P. Philippsen, and J.R. Pringle. 1998. Heterologous modules for efficient and versatile PCR-based gene targeting in Schizosaccharomyces pombe. *Yeast*. 14:943–951. https://doi.org/10.1002/(SICI)1097-0061(199807)14:10<943::AID-YEA292>3.0.CO;2-Y

Bhavsar-Jog, Y.P., and E. Bi. 2017. Mechanics and regulation of cytokinesis in budding yeast. *Semin. Cell Dev. Biol.* 66:107–118. https://doi.org/10.1016/j.semcdb.2016.12.010

Bidlingmaier, S., E.L. Weiss, C. Seidel, D.G. Drubin, and M. Snyder. 2001. The Cbk1p pathway is important for polarized cell growth and cell separation in Saccharomyces cerevisiae. *Mol. Cell. Biol.* 21:2449–2462. https://doi.org/10.1128/MCB.21.7.2449-2462.2001

Brace, J.L., M.D. Doerfler, and E.L. Weiss. 2019. A cell separation checkpoint that enforces the proper order of late cytokinetic events. *J. Cell Biol.* 218:150–170. https://doi.org/10.1083/jcb.201805100

Chen, X., K. Wang, T. Svitkina, and E. Bi. 2020. Critical roles of a RhoGEF-anillin module in septin architectural remodeling during cytokinesis. *Curr. Biol.* 30:1477–1490.e3. https://doi.org/10.1016/j.cub.2020.02.023

Chiou, J.G., M.K. Balasubramanian, and D.J. Lew. 2017. Cell polarity in yeast. *Annu. Rev. Cell Dev. Biol.* 33:77–101. https://doi.org/10.1146/annurev-cellbio-100616-060856

Chollet, J., A. Dünkler, A. Bäuerle, L. Vivero-Pol, M.A. Mulaw, T. Gronemeyer, and N. Johnsson. 2020. Cdc24 interacts with septins to create a positive feedback loop during bud site assembly in yeast. *J. Cell Sci.* 133:jcs240283. https://doi.org/10.1242/jcs.240283

Colman-Lerner, A., T.E. Chin, and R. Brent. 2001. Yeast Cbk1 and Mob2 activate daughter-specific genetic programs to induce asymmetric cell fates. *Cell*. 107:739–750. https://doi.org/10.1016/S0092-8674(01)00596-7

DeMarini, D.J., A.E. Adams, H. Fares, C. De Virgilio, G. Valle, J.S. Chuang, and J.R. Pringle. 1997. A septin-based hierarchy of proteins required for localized deposition of chitin in the Saccharomyces cerevisiae cell wall. *J. Cell Biol.* 139:75–93. https://doi.org/10.1083/jcb.139.1.75

DeMay, B.S., X. Bai, L. Howard, P. Occhipinti, R.A. Meseroll, E.T. Spiliotis, R. Oldenbourg, and A.S. Gladfelter. 2011. Septin filaments exhibit a dynamic, paired organization that is conserved from yeast to mammals. *J. Cell Biol.* 193:1065–1081. https://doi.org/10.1083/jcb.201012143

Devrekanli, A., M. Foltman, C. Roncero, A. Sanchez-Diaz, and K. Labib. 2012. Inn1 and Cyk3 regulate chitin synthase during cytokinesis in budding yeasts. *J. Cell Sci.* 125:5453–5466. https://doi.org/10.1242/jcs.109157

Dobbelaere, J., and Y. Barral. 2004. Spatial coordination of cytokinetic events by compartmentalization of the cell cortex. *Science*. 305:393–396. https://doi.org/10.1126/science.1099892

Dobbelaere, J., M.S. Gentry, R.L. Hallberg, and Y. Barral. 2003. Phosphorylation-dependent regulation of septin dynamics during the cell cycle. *Dev. Cell*. 4:345–357. https://doi.org/10.1016/S1534-5807(03)00061-3

Dohmen, R.J., R. Stappen, J.P. McGrath, H. Forrová, J. Kolarov, A. Goffeau, and A. Varshavsky. 1995. An essential yeast gene encoding a homolog of ubiquitin-activating enzyme. *J. Biol. Chem.* 270:18099–18109. https://doi.org/10.1074/jbc.270.30.18099

Dünkler, A., M. Leda, J.M. Kromer, J. Neller, T. Gronemeyer, A.B. Goryachev, and N. Johnsson. 2021. Type V myosin focuses the polarisome and shapes the tip of yeast cells. *J. Cell Biol.* 220:e202006193. https://doi.org/10.1083/jcb.202006193

Dünkler, A., J. Müller, and N. Johnsson. 2012. Detecting protein-protein interactions with the Split-Ubiquitin sensor. *Methods Mol. Biol.* 786:115–130. https://doi.org/10.1007/978-1-61779-292-2_7

Elmore, Z.C., M. Donaher, B.C. Matson, H. Murphy, J.W. Westerbeck, and O. Kerscher. 2011. Sumo-dependent substrate targeting of the SUMO protease Ulp1. *BMC Biol.* 9:74–7007. https://doi.org/10.1186/1741-7007-9-74

Ewers, H. 2011. Septin pairs, a complex choreography. *J. Cell Biol.* 193:959–961. https://doi.org/10.1083/jcb.201105076

Fang, X., J. Luo, R. Nishihama, C. Wloka, C. Dravis, M. Travaglia, M. Iwase, E.A. Vallen, and E. Bi. 2010. Biphasic targeting and cleavage furrow ingression directed by the tail of a myosin II. *J. Cell Biol.* 191:1333–1350. https://doi.org/10.1083/jcb.201005134

Foltman, M., I. Molist, I. Arcones, C. Sacristan, Y. Filali-Mouncef, C. Roncero, and A. Sanchez-Diaz. 2016. Ingression progression complexes control extracellular matrix remodelling during cytokinesis in budding yeast. *PLoS Genet.* 12:e1005864. https://doi.org/10.1371/journal.pgen.1005864

Fuentes, D., M. Molina, U. Chorostecki, S. Capella-Gutiérrez, M. Marcet-Houben, and T. Gabaldón. 2022. PhylomeDB V5: An expanding repository for genome-wide catalogues of annotated gene phylogenies. *Nucleic Acids Res.* 50:D1062–D1068. https://doi.org/10.1093/nar/gkab966

Glomb, O., Y. Wu, L. Rieger, D. Rüthnick, M.A. Mulaw, and N. Johnsson. 2020. The cell polarity proteins Boi1 and Boi2 direct an actin nucleation complex to sites of exocytosis in Saccharomyces cerevisiae. *J. Cell Sci.* 133:jcs237982. https://doi.org/10.1242/jcs.237982

Gohlke, S., D. Heine, H.P. Schmitz, and H. Merzendorfer. 2018. Septin-associated protein kinase Gin4 affects localization and phosphorylation of Chs4, the regulatory subunit of the Baker's yeast chitin synthase III complex. *Fungal Genet. Biol.* 117:11–20. https://doi.org/10.1016/j.fgb.2018.05.002

Grabińska, K.A., P. Magnelli, and P.W. Robbins. 2007. Prenylation of Saccharomyces cerevisiae Chs4p affects chitin synthase III activity and chitin chain length. *Eukaryot. Cell.* 6:328–336. https://doi.org/10.1128/EC.00203-06

Grinhagens, S., A. Dunkler, Y. Wu, L. Rieger, P. Brenner, T. Gronemeyer, M.A. Mulaw, and N. Johnsson. 2020. A time-resolved interaction analysis of Bem1 reconstructs the flow of Cdc42 during polar growth. *Life Sci. Alliance*. 3. e202000813. https://doi.org/10.26508/lsa.202000813

Hannich, J.T., A. Lewis, M.B. Kroetz, S.J. Li, H. Heide, A. Emili, and M. Hochstrasser. 2005. Defining the SUMO-modified proteome by multiple approaches in Saccharomyces cerevisiae. *J. Biol. Chem.* 280:4102–4110. https://doi.org/10.1074/jbc.M413209200

Hruby, A., M. Zapatka, S. Heucke, L. Rieger, Y. Wu, U. Nussbaumer, S. Timmermann, A. Dünkler, and N. Johnsson. 2011. A constraint network of interactions: Protein-protein interaction analysis of the yeast type II phosphatase Ptc1p and its adaptor protein Nbp2p. *J. Cell Sci.* 124:35–46. https://doi.org/10.1242/jcs.077065

Janke, C., M.M. Magiera, N. Rathfelder, C. Taxis, S. Reber, H. Maekawa, A. Moreno-Borchart, G. Doenges, E. Schwob, E. Schiebel, and M. Knop. 2004. A versatile toolbox for PCR-based tagging of yeast genes: New fluorescent proteins, more markers and promoter substitution cassettes. *Yeast*. 21:947–962. https://doi.org/10.1002/yea.1142

Johnson, E.S., and G. Blobel. 1999. Cell cycle-regulated attachment of the ubiquitin-related protein SUMO to the yeast septins. *J. Cell Biol.* 147:981–994. https://doi.org/10.1083/jcb.147.5.981

Johnson, E.S., and A.A. Gupta. 2001. An E3-like factor that promotes SUMO conjugation to the yeast septins. *Cell*. 106:735–744. https://doi.org/10.1016/S0092-8674(01)00491-3

Johnsson, N., and A. Varshavsky. 1994. Split ubiquitin as a sensor of protein interactions in vivo. *Proc. Natl. Acad. Sci. USA*. 91:10340–10344. https://doi.org/10.1073/pnas.91.22.10340

Jumper, J., R. Evans, A. Pritzel, T. Green, M. Figurnov, O. Ronneberger, K. Tunyasuvunakool, R. Bates, A. Žídek, A. Potapenko, et al. 2021. Highly accurate protein structure prediction with AlphaFold. *Nature*. 596:583–589. https://doi.org/10.1038/s41586-021-03819-2

Kozubowski, L., H. Panek, A. Rosenthal, A. Bloecher, D.J. DeMarini, and K. Tatchell. 2003. A Bni4-Glc7 phosphatase complex that recruits chitin synthase to the site of bud emergence. *Mol. Biol. Cell*. 14:26–39. https://doi.org/10.1091/mbc.e02-06-0373

Larson, J.R., J.P. Bharucha, S. Ceaser, J. Salamon, C.J. Richardson, S.M. Rivera, and K. Tatchell. 2008. Protein phosphatase type 1 directs chitin synthesis at the bud neck in Saccharomyces cerevisiae. *Mol. Biol. Cell*. 19:3040–3051. https://doi.org/10.1091/mbc.e08-02-0130

Laughery, M.F., T. Hunter, A. Brown, J. Hoopes, T. Ostbye, T. Shumaker, and J.J. Wyrick. 2015. New vectors for simple and streamlined CRISPR-Cas9 genome editing in Saccharomyces cerevisiae. *Yeast*. 32:711–720. https://doi.org/10.1002/yea.3098

Lewis, A., R. Felberbaum, and M. Hochstrasser. 2007. A nuclear envelope protein linking nuclear pore basket assembly, SUMO protease regulation, and mRNA surveillance. *J. Cell Biol.* 178:813–827. https://doi.org/10.1083/jcb.200702154

Makhnevych, T., C. Ptak, C.P. Lusk, J.D. Aitchison, and R.W. Wozniak. 2007. The role of karyopherins in the regulated sumoylation of septins. *J. Cell Biol.* 177:39–49. https://doi.org/10.1083/jcb.200608066

Marquardt, J., X. Chen, and E. Bi. 2021. Septin assembly and remodeling at the cell division site during the cell cycle. *Front. Cell Dev. Biol.* 9:793920. https://doi.org/10.3389/fcell.2021.793920

Meissner, D., J. Odman-Naresh, I. Vogelpohl, and H. Merzendorfer. 2010. A novel role of the yeast CaaX protease Ste24 in chitin synthesis. *Mol. Biol. Cell*. 21:2425–2433. https://doi.org/10.1091/mbc.e10-01-0080

Meitinger, F., M.E. Boehm, A. Hofmann, B. Hub, H. Zentgraf, W.D. Lehmann, and G. Pereira. 2011. Phosphorylation-dependent regulation of the F-BAR protein Hof1 during cytokinesis. *Genes Dev.* 25:875–888. https://doi.org/10.1101/gad.622411

Meitinger, F., and S. Palani. 2016. Actomyosin ring driven cytokinesis in budding yeast. *Semin. Cell Dev. Biol.* 53:19–27. https://doi.org/10.1016/j.semcdb.2016.01.043

Meitinger, F., S. Palani, B. Hub, and G. Pereira. 2013. Dual function of the NDR-kinase Dbf2 in the regulation of the F-BAR protein Hof1 during cytokinesis. *Mol. Biol. Cell*. 24:1290–1304. https://doi.org/10.1091/mbc.e12-08-0608

Neller, J., A. Dünkler, R. Rösler, and N. Johnsson. 2015. A protein complex containing Epo1p anchors the cortical endoplasmic reticulum to the yeast bud tip. *J. Cell Biol.* 208:71–87. https://doi.org/10.1083/jcb.201407126

Oh, Y., J.H. Schreiter, H. Okada, C. Wloka, S. Okada, D. Yan, X. Duan, and E. Bi. 2017. Hof1 and Chs4 interact via F-BAR domain and sel1-like repeats to control extracellular matrix deposition during cytokinesis. *Curr. Biol.* 27:2878–2886.e5. https://doi.org/10.1016/j.cub.2017.08.032

Okada, H., B. MacTaggart, Y. Ohya, and E. Bi. 2020. The kinetic landscape and interplay of protein networks in cytokinesis. *iScience*. 24:101917. https://doi.org/10.1016/j.isci.2020.101917

Ong, K., C. Wloka, S. Okada, T. Svitkina, and E. Bi. 2014. Architecture and dynamic remodelling of the septin cytoskeleton during the cell cycle. *Nat. Commun.* 5:5698. https://doi.org/10.1038/ncomms6698

Onishi, M., N. Ko, R. Nishihama, and J.R. Pringle. 2013. Distinct roles of Rho1, Cdc42, and Cyk3 in septum formation and abscission during yeast cytokinesis. *J. Cell Biol.* 202:311–329. https://doi.org/10.1083/jcb.201302001

Ono, N., T. Yabe, M. Sudoh, T. Nakajima, T. Yamada-Okabe, M. Arisawa, and H. Yamada-Okabe. 2000. The yeast Chs4 protein stimulates the trypsin-sensitive activity of chitin synthase 3 through an apparent protein-protein interaction. *Microbiology*. 146:385–391. https://doi.org/10.1099/00221287-146-2-385

Ostapenko, D., J.L. Burton, and M.J. Solomon. 2012. Identification of anaphase promoting complex substrates in S. cerevisiae. *PLoS One*. 7:e45895. https://doi.org/10.1371/journal.pone.0045895

Panse, V.G., B. Küster, T. Gerstberger, and E. Hurt. 2003. Unconventional tethering of Ulp1 to the transport channel of the nuclear pore complex by karyopherins. *Nat. Cell Biol.* 5:21–27. https://doi.org/10.1038/ncb893

Pruyne, D., and A. Bretscher. 2000. Polarization of cell growth in yeast. I. Establishment and maintenance of polarity states. *J. Cell Sci.* 113:365–375. https://doi.org/10.1242/jcs.113.3.365

Reyes, A., M. Sanz, A. Duran, and C. Roncero. 2007. Chitin synthase III requires Chs4p-dependent translocation of Chs3p into the plasma membrane. *J. Cell Sci.* 120:1998–2009. https://doi.org/10.1242/jcs.005124

Ribet, D., S. Boscaini, C. Cauvin, M. Siguier, S. Mostowy, A. Echard, and P. Cossart. 2017. SUMOylation of human septins is critical for septin filament bundling and cytokinesis. *J. Cell Biol.* 216:4041–4052. https://doi.org/10.1083/jcb.201703096

Schindelin, J., I. Arganda-Carreras, E. Frise, V. Kaynig, M. Longair, T. Pietzsch, S. Preibisch, C. Rueden, S. Saalfeld, B. Schmid, et al. 2012. Fiji: An open-source platform for biological-image analysis. *Nat. Methods*. 9:676–682. https://doi.org/10.1038/nmeth.2019

Schneider, C., J. Grois, C. Renz, T. Gronemeyer, and N. Johnsson. 2013. Septin rings act as a template for myosin higher-order structures and inhibit redundant polarity establishment. *J. Cell Sci.* 126:3390–3400. https://doi.org/10.1242/jcs.125302

Schneider, C.A., W.S. Rasband, and K.W. Eliceiri. 2012. NIH image to ImageJ: 25 years of image analysis. *Nat. Methods*. 9:671–675. https://doi.org/10.1038/nmeth.2089

Shih, J.L., S.L. Reck-Peterson, R. Newitt, M.S. Mooseker, R. Aebersold, and I. Herskowitz. 2005. Cell polarity protein Spa2P associates with proteins involved in actin function in Saccharomyces cerevisiae. *Mol. Biol. Cell*. 16:4595–4608. https://doi.org/10.1091/mbc.e05-02-0108

Snyder, M. 1989. The SPA2 protein of yeast localizes to sites of cell growth. *J. Cell Biol.* 108:1419–1429. https://doi.org/10.1083/jcb.108.4.1419

Takahashi, Y., M. Iwase, M. Konishi, M. Tanaka, A. Toh-e, and Y. Kikuchi. 1999. Smt3, a SUMO-1 homolog, is conjugated to Cdc3, a component of septin rings at the mother-bud neck in budding yeast. *Biochem. Biophys. Res. Commun.* 259:582–587. https://doi.org/10.1006/bbrc.1999.0821

Takahashi, Y., T. Kahyo, A. Toh-E, H. Yasuda, and Y. Kikuchi. 2001. Yeast Ulli1/Siz1 is a novel SUMO1/Smt3 ligase for septin components and functions as an adaptor between conjugating enzyme and substrates. *J. Biol. Chem.* 276:48973–48977. https://doi.org/10.1074/jbc.M109295200

Takahashi, Y., J. Mizoi, A. Toh-E, and Y. Kikuchi. 2000. Yeast Ulp1, an Smt3-specific protease, associates with nucleoporins. *J. Biochem.* 128:723–725. https://doi.org/10.1093/oxfordjournals.jbchem.a022807

Tcheperegine, S.E., X.D. Gao, and E. Bi. 2005. Regulation of cell polarity by interactions of Msb3 and Msb4 with Cdc42 and polarisome components. *Mol. Cell. Biol.* 25:8567–8580. https://doi.org/10.1128/MCB.25.19.8567-8580.2005

Tully, G.H., R. Nishihama, J.R. Pringle, and D.O. Morgan. 2009. The anaphase-promoting complex promotes actomyosin-ring disassembly during cytokinesis in yeast. *Mol. Biol. Cell*. 20:1201–1212. https://doi.org/10.1091/mbc.e08-08-0822

Uzunova, K., K. Göttsche, M. Miteva, S.R. Weisshaar, C. Glanemann, M. Schnellhardt, M. Niessen, H. Scheel, K. Hofmann, E.S. Johnson, et al. 2007. Ubiquitin-dependent proteolytic control of SUMO conjugates. *J. Biol. Chem.* 282:34167–34175. https://doi.org/10.1074/jbc.M706505200

Valtz, N., and I. Herskowitz. 1996. Pea2 protein of yeast is localized to sites of polarized growth and is required for efficient mating and bipolar budding. *J. Cell Biol.* 135:725–739. https://doi.org/10.1083/jcb.135.3.725

Vrabioiu, A.M., and T.J. Mitchison. 2006. Structural insights into yeast septin organization from polarized fluorescence microscopy. *Nature*. 443:466–469. https://doi.org/10.1038/nature05109

Weiss, E.L., C. Kurischko, C. Zhang, K. Shokat, D.G. Drubin, and F.C. Luca. 2002. The Saccharomyces cerevisiae Mob2p-Cbk1p kinase complex promotes polarized growth and acts with the mitotic exit network to facilitate daughter cell-specific localization of Ace2p transcription factor. *J. Cell Biol.* 158:885–900. https://doi.org/10.1083/jcb.200203094

Weiss, E.L. 2012. Mitotic exit and separation of mother and daughter cells. *Genetics*. 192:1165–1202. https://doi.org/10.1534/genetics.112.145516

Wittke, S., N. Lewke, S. Müller, and N. Johnsson. 1999. Probing the molecular environment of membrane proteins in vivo. *Mol. Biol. Cell*. 10:2519–2530. https://doi.org/10.1091/mbc.10.8.2519

Wloka, C., R. Nishihama, M. Onishi, Y. Oh, J. Hanna, J.R. Pringle, M. Krauss, and E. Bi. 2011. Evidence that a septin diffusion barrier is dispensable for cytokinesis in budding yeast. *Biol. Chem.* 392:813–829. https://doi.org/10.1515/BC.2011.083

Woods, B.L., and A.S. Gladfelter. 2021. The state of the septin cytoskeleton from assembly to function. *Curr. Opin. Cell Biol.* 68:105–112. https://doi.org/10.1016/j.ceb.2020.10.007

Wu, Y., Q. Li, and X.Z. Chen. 2007. Detecting protein-protein interactions by Far western blotting. *Nat. Protoc.* 2:3278–3284. https://doi.org/10.1038/nprot.2007.459

Supplemental material

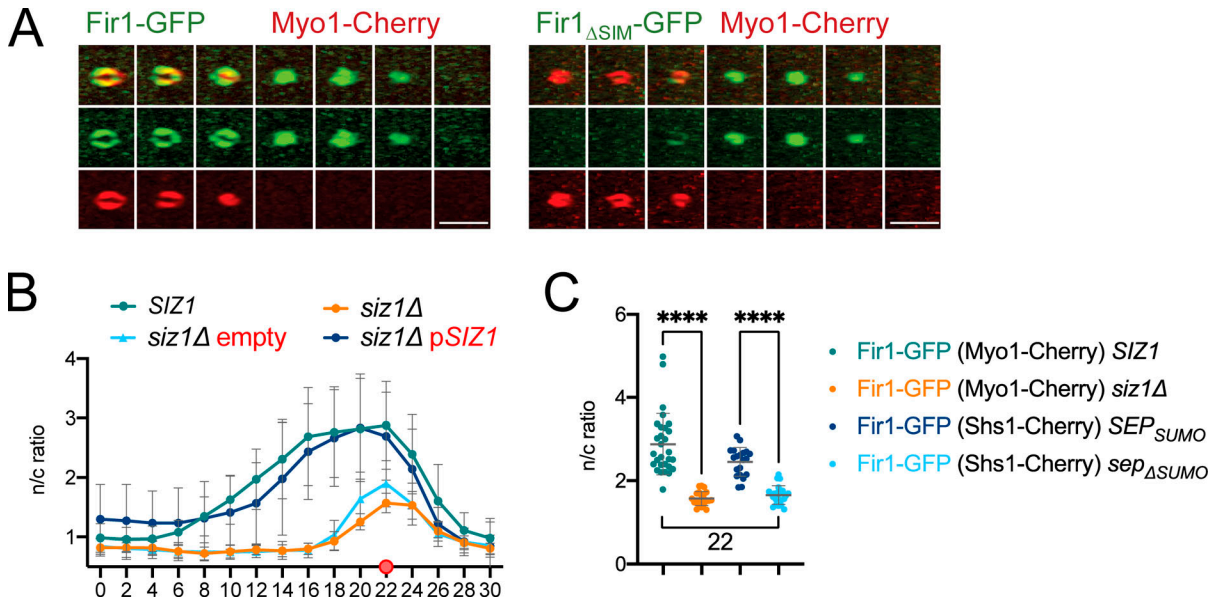

Figure S1. **Septin sumoylation attaches Fir1 to the septin ring. (A)** Deconvoluted images of the bud neck of cells coexpressing Fir1-GFP (left panels) or Fir1$_{\Delta SIM}$-GFP (right panels) together with Myo1-Cherry, taken every 2 min, starting 6 min before Myo1 contraction is complete. Overlay, GFP and Cherry channels are shown in the top, middle, and lower panels. Scale bars = 3 µm. **(B)** As in Fig. 1 C but showing the complementation of *siz1*Δ cells. Coexpression of plasmid-encoded *SIZ1* in *siz1*Δ cells (p*SIZ1*; *n* = 25) rescued Fir1-GFP signal timing and intensity, while the empty vector had no effect (empty plasmid; *n* = 23). **(C)** Statistical evaluation of differences in signal intensities of Fir1-GFP in wild type, sep$_{\Delta sumo}$, and *siz1*Δ cells at time point 22 of Fig. 1 E. ****P < 0.0001. Error bars, SD.

https://doi.org/10.1083/jcb.202301027

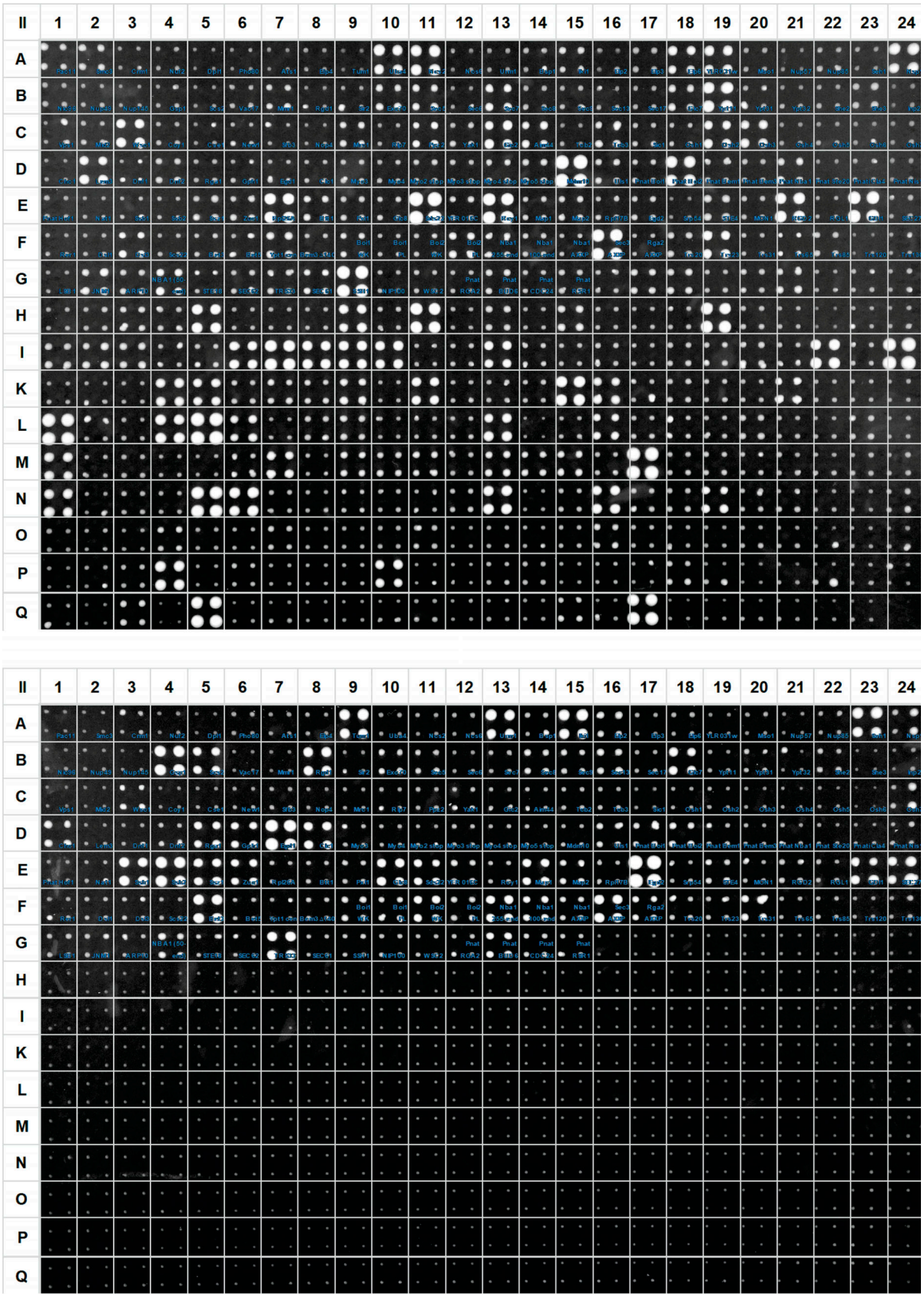

Figure S2. **Split-Ub interaction assay of 540 yeast strains coexpressing P_{MET17}-Fir1CRU each with a different N_{ub} fusion protein.** For every strain, cells of four independent matings were spotted as quadruplets on SD medium containing 5-FOA, 50 µM copper sulfate, and 0 M methionine. Shown is the growth of the diploid yeast cells after 2 d at 30°C. Growth indicates protein–protein interactions.

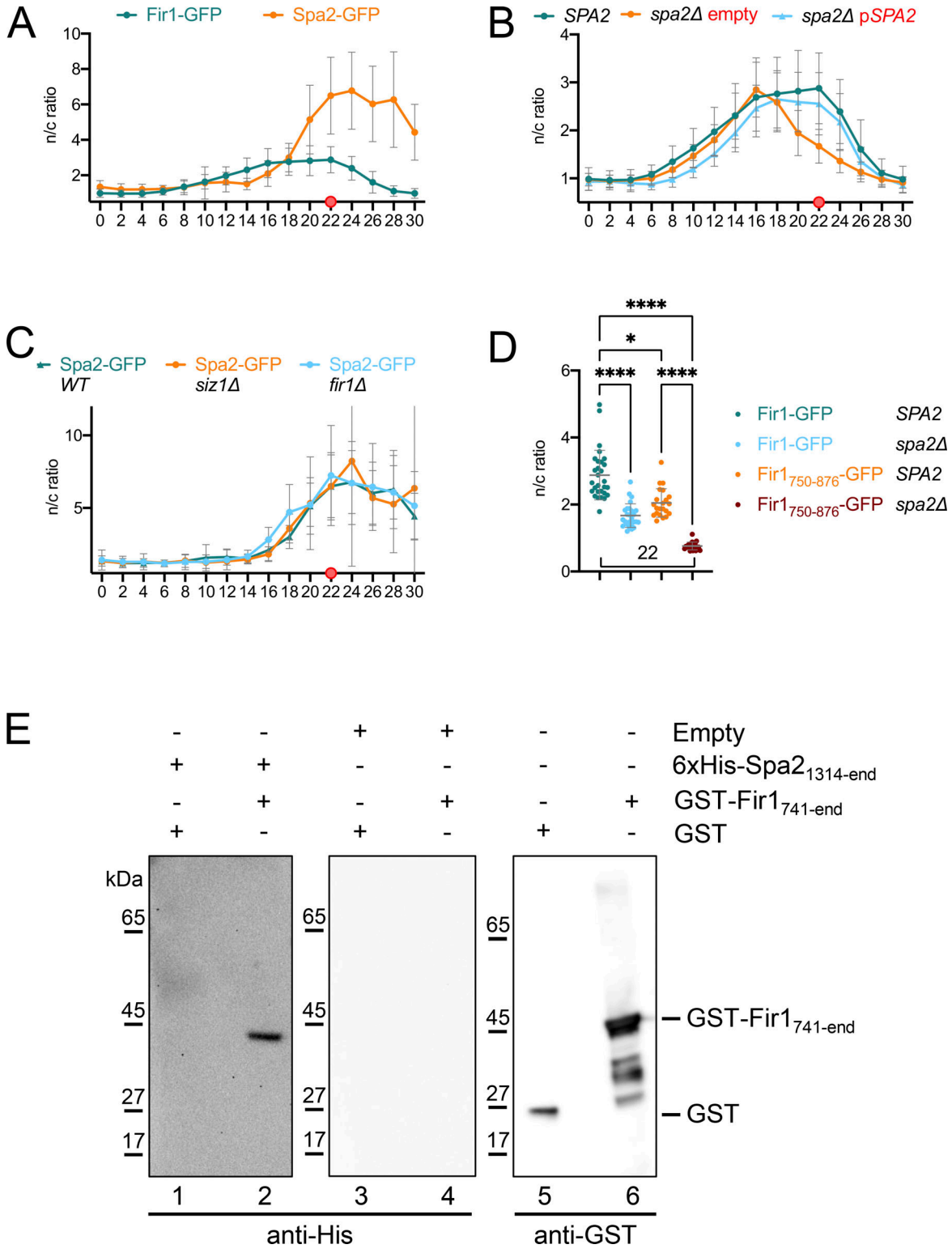

Figure S3. **Spa2 recruits Fir1 into the space between the SSDR. (A)** As in Fig. 1 C but with cells co-expressing Fir1-GFP, or Spa2-GFP with Myo1-Cherry. **(B)** As in Fig. 1 C but showing the complementation of the reduction of the Fir1-GFP bud neck signal in *spa2*Δ cells. Co-expression of plasmid-encoded *SPA2* (p*SPA2*, *n* = 28) rescued timing and intensity of the Fir1-GFP signal in *spa2*Δ cells, while the empty vector had no effect (empty plasmid, *n* = 26). **(C)** As in Fig. 1 C. The Spa2-GFP signal at the bud neck remains unaffected in timing and intensity by the deletion of *SIZ1* (*siz1*Δ; *n* = 17) or *FIR1* (*fir1*Δ; *n* = 13). **(D)** Statistical evaluation of differences in signal intensities at time point 22 of Fig. 2 D between Fir1-GFP in wild type and *spa2*Δ cells, between $Fir1_{750-876}$-GFP in wild type and *spa2*Δ cells, and between Fir1-GFP and $Fir1_{750-876}$-GFP in wild type and *spa2*Δ cells. ****P < 0.0001; *P = 0.0174. Error bars, SD. **(E)** Equal amounts of *E. coli* extracts containing GST (lanes 1, 3, 5), or GST-$Fir1_{741-876}$ (2, 4, 6) were separated by SDS-PAGE, transferred to nitrocellulose, and incubated with extracts from *E. coli* expressing no additional protein (lanes 3, 4) or 6xHis-$Spa2_{1,324-end}$ (lanes 1, 2). GST or 6xHis fusions were subsequently detected by anti-GST (lanes 5, 6) or anti-His antibodies (lanes 1–4). Source data are available for this figure: SourceData FS3.

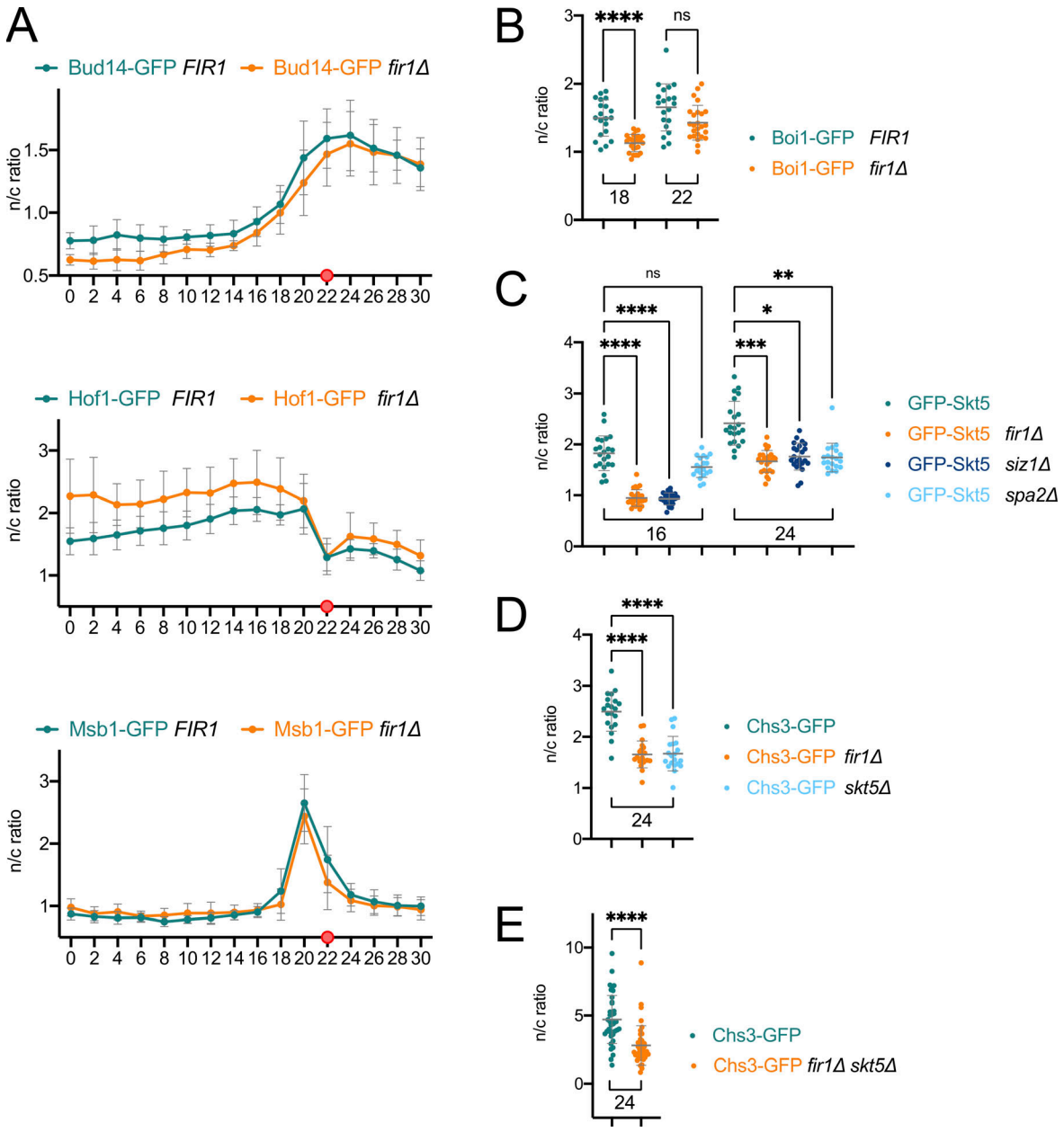

Figure S4. **Targeting of Bud14, Hof1, and Msb1 is not affected by Fir1. (A)** As in Fig. 1 C but with cells co-expressing Myo1-Cherry with Bud14-GFP (upper panel; wild type *n* = 9; *fir1*Δ *n* = 8), Hof1-GFP (middle panel; wild type *n* = 17; *fir1*Δ *n* = 22), or Msb1-GFP (lower panel: wild type *n* = 13; *fir1*Δ n = 10) with or without *FIR1*. **(B)** Statistical evaluation of differences in signal intensities between Boi1-GFP in the presence and absence of *FIR1* at time points 18 and 22 of Fig. 4 B. ****P < 0.0001; ns, not significant. **(C)** Statistical evaluation of differences in signal intensities between GFP-Skt5 in wild-type cells and strains lacking *FIR1*, *SIZ1*, or *SPA2* at time points 16 and 24 of Fig. 4 C. ****P < 0.0001; ***P = 0.0005; **P = 0.0066; *P = 0.0166; ns, not significant. **(D)** Statistical evaluation of differences in signal intensities between Chs3-GFP in the presence and absence of *FIR1* or *SKT5* at time point 24 of Fig. 4 E. ****P < 0.0001. **(E)** As in D but for Chs3-GFP in the presence and absence of *FIR1* and *SKT5* at time point 24 of Fig. 4 F. ****P < 0.0001. Error bars, SD.

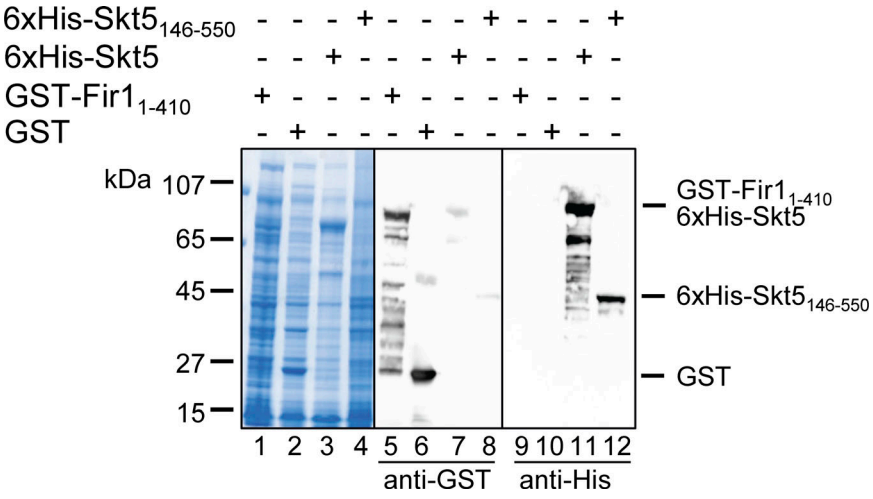

Figure S5. **Inputs for** Fig. 5 B**.** *E. coli* extracts expressing GST-Fir1$_{1–410}$ (lanes 1, 5, 9), GST (lanes 2, 6, 10), 6xHis-Skt5 (lanes 3, 7, 11), or 6xHis-Skt5$_{146–550}$ (lanes 4, 8, 12) were separated by SDS-PAGE and either stained with Coomassie (lanes 1–4), or transferred to nitrocellulose and stained with anti-GST (lanes 5–8), or anti-His antibodies (lanes 9–12). Source data are available for this figure: SourceData FS5.

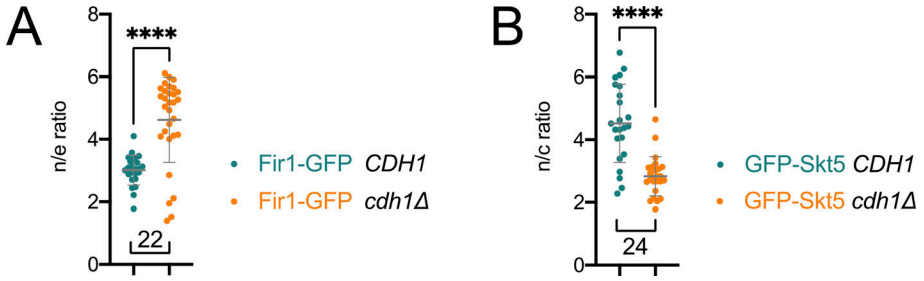

Figure S6. **Cdh1 deltetion significantly affects Fir1 and Skt5 localization. (A)** Statistical evaluation of differences in signal intensities between Fir1-GFP in the presence and absence of *CDH1* at time point 22 of Fig. 6 A. ****P < 0.0001. **(B)** Statistical evaluation of the differences in signal intensities between GFP-Skt5 in the presence and absence of *CDH1* at time point 24 of Fig. 6 D. ****P < 0.0001.

Provided online are four tables. Table S1 lists interaction partners of Fir1. Table S2 lists *S. cerevisiae* strains used and created in this study. Table S3 lists constructed plasmids in this study. Table S4 lists primers used and created in this study.